

See discussions, stats, and author profiles for this publication at: <https://www.researchgate.net/publication/238122111>

# Transition State Resonances in the Reaction $\text{Cl} + \text{H}_2 \rightarrow \text{HCl} + \text{H}$

ARTICLE in THE JOURNAL OF PHYSICAL CHEMISTRY A · MARCH 1999

Impact Factor: 2.69 · DOI: 10.1021/jp984549k

CITATIONS

17

READS

9

4 AUTHORS, INCLUDING:



Thomas C Allison

National Institute of Standards and Technolo...

53 PUBLICATIONS 871 CITATIONS

SEE PROFILE



David W. Schwenke

NASA

256 PUBLICATIONS 7,138 CITATIONS

SEE PROFILE



Donald Truhlar

University of Minnesota Twin Cities

1,342 PUBLICATIONS 81,184 CITATIONS

SEE PROFILE

Transition State Resonances in the Reaction  $\text{Cl} + \text{H}_2 \rightarrow \text{HCl} + \text{H}$ Jay Srinivasan,<sup>†</sup> Thomas C. Allison,<sup>†</sup> David W. Schwenke,<sup>‡</sup> and Donald G. Truhlar<sup>\*,†</sup>Department of Chemistry and Supercomputer Institute, University of Minnesota,  
Minneapolis, Minnesota 55455-0431, and NASA Ames Research Center, Mail Stop 230-3,  
Moffett Field, California 94035-1000

Received: November 30, 1998; In Final Form: January 11, 1999

This paper discusses converged quantum mechanical scattering calculations for the reaction  $\text{Cl} + \text{H}_2 \rightarrow \text{HCl} + \text{H}$  and its reverse and analyzes them for the properties of quantized dynamical bottlenecks controlling the total and state-specific microcanonical-ensemble rate constants. These rate constants show clear evidence for quantized transition states. We assign bend and stretch quantum numbers to the transition states for total angular momentum  $J = 0$  with parity  $P = +1$ , for  $J = 1$  with  $P = +1$  and  $-1$ , and for  $J = 2$  and  $6$  with  $P = +1$ . Then, state-specific densities of reactive states (transition state spectra) are examined to obtain a detailed picture of the reaction. A quantal estimate of the rotational constant,  $B$ , for several different transition states is obtained by comparing transition state energies at different values of the total angular momentum. These quantal estimates are in good agreement with the values calculated from the moments of inertia, and this enables us to interpret the results in terms of state-dependent geometries for the individual dynamical bottlenecks. By treating the transition states as poles in the scattering matrix, we also obtain estimates for the lifetimes of the states. The  $JP$ -specific rate coefficients, the reactant-state-specific rate coefficients, and the contribution from each transition state to the  $JP$ -specific and the reactant-state-specified rate coefficient are also calculated and the trends analyzed. These trends help explain the dependence of the rate coefficient on initial vibrational and rotational quantum numbers.

## I. Introduction

Recent work has established that the flux through dynamical bottleneck regions of potential energy surfaces is gated by a series of quantum mechanical resonances that correspond to discrete steps in the cumulative reaction probability as the energy is raised.<sup>1–3</sup> The steps are broadened by quantum mechanical tunneling. Several reviews are available, covering both theory and experiment.<sup>4–7</sup> The resonances, like all resonances, correspond to poles of the scattering matrix (S matrix).<sup>8–13</sup> The classical analogues of the resonances are periodic orbits for systems with two degrees of freedom<sup>12</sup> and reduced-dimensional tori or quasiperiodic orbits in systems with more degrees of freedom.<sup>14</sup>

Atom–diatom reactions have six vibrational degrees of freedom, excluding overall translation, and when the saddle point structure is collinear, these are typically taken as four vibrations and two rotations. The transition state resonances of several atom–diatom systems have been analyzed in great detail with assignments of vibrational quantum numbers, energies, and resonance widths in the energy domain.<sup>1–5,15–18</sup> The widths in the energy domain may be related to widths of effective tunneling barriers in coordinate space and to the lifetimes of the quantum mechanical metastable states.<sup>4</sup>

The resonance states may be understood most intuitively as quantized levels of variational transition states, which may in turn be visualized as global maxima of state-specific effective potential curves as functions of a reaction coordinate.<sup>2</sup> A very interesting feature in the  $\text{O} + \text{H}_2$  and  $\text{Cl} + \text{H}_2$  systems is the existence of additional resonances corresponding to local maxima of the effective potential curves that are not global

maxima. These are called supernumerary transition states, and they have been further classified into supernumeraries of the first and second kinds.<sup>15</sup> The supernumerary phenomena have been fully analyzed in the  $\text{O} + \text{H}_2$  system,<sup>15</sup> but so far only a preliminary analysis has been available for  $\text{Cl} + \text{H}_2$ .<sup>5,19</sup>

For a microcanonical ensemble of systems with energy  $E$ , total angular momentum  $J$ , parity  $P$ , and permutational symmetry  $S$ , the rate constant is given by

$$k^{JPS} = \frac{N^{JPS}(E)}{h\phi^{R,JPS}(E)} \quad (1)$$

where  $h$  is Planck's constant,  $\phi^{R,JPS}(E)$  is the density of states per unit energy and volume for reactants, and  $N^{JPS}(E)$  is the cumulative reaction probability (CRP) given by

$$N^{JPS}(E) = \sum_{n \in R} \sum_{n' \in P} P_{nn'}^{JPS} \quad (2)$$

where  $n$  is a set of quantum numbers ( $\alpha$ ,  $\nu$ ,  $j$ , and  $l$ ) specifying a reactant (R) state,  $n'$  is a set of quantum numbers ( $\alpha'$ ,  $\nu'$ ,  $j'$ , and  $l'$ ) specifying a product (P) state,  $P_{nn'}^{JPS}$  is a state-to-state reaction probability,  $\alpha$  and  $\alpha'$  are arrangement quantum numbers (with  $\alpha = 1$  for reactant  $\text{Cl} + \text{H}_2$  states and  $\alpha' = 2$  or  $3$  for product  $\text{HCl} + \text{H}$  states),  $\nu$  and  $\nu'$  are vibrational quantum numbers,  $j$  and  $j'$  are rotational quantum numbers, and  $l$  and  $l'$  are orbital angular momentum quantum numbers. Notice that  $\phi^{R,JPS}(E)$  is purely an equilibrium quantity; hence all the dynamical information in  $k^{JPS}(E)$  is contained in the CRP.

The present paper presents well-converged CRPs for the  $\text{Cl} + \text{H}_2$  reaction and its reverse ( $\text{HCl} + \text{H}$ ) for total angular momenta  $JPS = 0++$ ,  $1++$ ,  $1-+$ ,  $2++$ , and  $6++$  and analyzes them in terms of resonances corresponding to varia-

<sup>†</sup> University of Minnesota.<sup>‡</sup> NASA Ames Research Center.

tional and supernumerary transition states. In addition, we examine the implications of these transition state resonances for state-specific reactivity of both the forward and reverse reactions, questions explored most fully in previous work for  $\text{H} + \text{H}_2^{3,4}$  and  $\text{O} + \text{H}_2^{15}$ . All calculations in this paper employ the realistic G3 potential energy surface<sup>20</sup> (PES) for  $\text{ClH}_2$ , which has been shown<sup>19–22</sup> to lead to good agreement with experiment. The classical barrier height on this potential energy surface is 0.3417 eV for the forward reaction and 0.2111 eV for the reverse reaction.

Section II presents the computational methods. Section III has results, and these are analyzed and discussed in section IV. Section V presents concluding remarks.

## II. Computational Methods

**II.A. Scattering Calculations.** We used the outgoing wave variational principle<sup>23–27</sup> (OWVP) to calculate the quantum mechanical CRP of the reaction of  $\text{Cl}$  and  $\text{H}_2$ . Details of these calculations as well as a description of the methods and algorithms used have been presented previously.<sup>21</sup> As before, we used masses of 67384.72 au and 1837.153 au for  $^{37}\text{Cl}$  and  $^1\text{H}$ , respectively. We started with the data given in the supplementary information of ref 21. We also performed calculations of the CRP for values of the total angular momentum  $JPS = 1++$ ,  $1-+$ ,  $2++$ , and  $6++$  at energies from 0.33 to 0.99 eV, all with an energy spacing of 0.02 eV, and at energies from 1.0 to 1.1 eV at an energy spacing of 0.01 eV. For the new calculations, we used the same scattering basis set parameters and screening parameters as shown in set A of Table 2 of ref 21. By merging these new calculations with the data presented in ref 21, we have CRP data in the energy range from 0.32 to 1.1 eV at a energy spacing of 0.01 eV for the five combinations of quantum numbers:  $JPS = 0++$ ,  $1++$ ,  $1-+$ ,  $2++$ , and  $6++$ .

**II.B. Extraction of Transition-State Resonance Parameters.** For each  $JPS$  considered, we fit  $N^{JPS}(E)$  as a function of energy  $E$  to a cubic spline<sup>28</sup> function. The energy derivative  $dN^{JPS}(E)/dE$  of the spline fit to the CRP gives us the density of reactive states,<sup>2</sup> called  $\rho^{JPS}(E)$  or the DORS. We obtain the DORS curve by taking the first derivative of the spline fit to the CRP. The density of reactive states has structure that can be attributed to the presence of quantized transition states of the reaction.<sup>2</sup>

The features in the DORS plot that correspond to energy levels of the quantized transition state can be assigned to a set  $[\nu_1\nu_2^K]$  of transition state quantum numbers, where  $\nu_1$  and  $\nu_2$  are stretch and bend quantum numbers for motions transverse to the reaction coordinate and  $K$  is the vibrational angular momentum.<sup>29</sup> The vibrational angular momentum arises due to the superposition of the two degenerate bending vibrations of the triatomic system. Thus, if a harmonic bending vibration is excited by  $\nu_2$  quanta, the degree of degeneracy is  $\nu_2 + 1$ .<sup>29</sup> The state with zero-point vibration is nondegenerate. The values that the vibrational angular momentum quantum number  $K$  can take are  $K = \nu_2, \nu_2 - 2, \nu_2 - 4, \dots, 0$  or  $1$ , with the restriction that  $K \leq J$ , since any one component of the angular momentum can never exceed the total angular momentum. In addition, since the bending mode is doubly degenerate, each state with  $K > 0$  is doubly degenerate with one odd and one even parity component. Since we can perform parity-specific calculations, we can resolve the two parity components. For example, as we show later in section III, when  $J = 2$ ,  $\nu_1 = 0$ , and  $\nu_2 = 2$ , we obtain the doubly degenerate state  $[02^2]$ , with one component showing up in the even parity spectrum and the other in the

odd parity spectrum. We also obtain the  $[02^0]$  state giving a total degeneracy of 3 for the  $\nu_2 = 2$  excitation. The transition states differing in only the  $K$  values are in fact nondegenerate due to anharmonicity;<sup>29</sup> they are, however, too close in energy to be resolved in our calculations.<sup>5</sup> Thus, the  $[02^0]$  and  $[02^2]$  states overlap each other and are seen as just one feature. To stress this point, we designate the state as  $[02^{0,2}]$ . (Note that the  $K$  states are harder to resolve than the  $J$  states because  $K$  is not a conserved quantum number, and the different  $K$  states always appear as heavily overlapped features. In contrast, we can look at different  $J$  states in different spectra.)

The assignments can be made using a variety of considerations. We will use (i) information from semiclassically obtained vibrationally adiabatic (VA) curves<sup>30–33</sup> for the  $\text{Cl} + \text{H}_2$  reaction, (ii) a fit of the DORS curve to a sum of line shape functions corresponding to tunneling through effective parabolic barriers, and (iii) state-to-state reaction probabilities and their corresponding state-to-state DORSs.<sup>15</sup>

The VA curves are defined by the equation<sup>34</sup>

$$V_a(\nu_1, \nu_2, K, s) = V_{\text{MEP}}(s) + \epsilon_{\text{int}}(\nu_1, \nu_2, K, s) \quad (3)$$

where  $s$  is the distance along the reaction path, through isoinertial coordinates<sup>35</sup> with a reduced mass of  $\mu$  of 3484.32 amu.  $s = 0$  corresponds to the saddle point,  $V_{\text{MEP}}$  is the Born–Oppenheimer potential energy along the minimum energy reaction path (MEP), and  $\epsilon_{\text{int}}$  is the vibrational energy of the modes excluding motion along the reaction coordinate. The VA curves are obtained by using the program ABCRATE<sup>36</sup> wherein the MEP is calculated using the steepest descent method<sup>35</sup> on both sides of the saddle point, the quantized energies of the stretching modes are approximated by the WKB method,<sup>37,38</sup> and the quantized energies of the bends are obtained from a centrifugal oscillator treatment<sup>39,40</sup> using a quadratic-quartic fit to the two-dimensional potential for bending motions.

We can obtain an approximation to the DORS by using variational transition state theory<sup>34</sup> (VTST) corrected for the possibility of tunneling and for the fact that even the variational transition state may be an imperfect bottleneck. Using a parabolic effective energy barrier allows us to write an expression for the density of states as a sum of line shape functions for each transition state  $\gamma$  given by<sup>2</sup>

$$\rho^{JPS}(E) = \sum_{\gamma} \kappa_{\gamma} \rho_{\gamma}^{JPS}(E) = \sum_{\gamma} \frac{\kappa_{\gamma} \exp[(E_{\gamma} - E)/W_{\gamma}]}{W_{\gamma} \{1 + \exp[(E_{\gamma} - E)/W_{\gamma}]\}^2} \quad (4)$$

where  $W_{\gamma}$  is the width parameter of the resonance centered at  $E_{\gamma}$ , and  $\kappa_{\gamma}$  is a parameter that we may call the level-dependent transmission coefficient. Ideally,  $\kappa_{\gamma}$  should be unity (if the variational transition states were perfect dynamical bottlenecks).

State-specific spectra are also useful in assigning the quantum numbers to the transition states. The state-specific reaction probabilities are obtained by selectively summing the reaction probabilities over certain vibrational or rotational states. We note that the reactant state labels  $n$  denote a set of quantum numbers consisting of the initial arrangement quantum number  $\alpha$ , the diatomic vibrational quantum number  $\nu$ , the diatomic rotational quantum number  $j$ , and the orbital angular momentum quantum number  $l$ . Similarly  $n'$  denotes  $\alpha'$ ,  $\nu'$ ,  $j'$ , and  $l'$ . Thus, to obtain vibrationally specific reaction probabilities,  $N_{\nu\nu'}^{JPS}$ , we sum over the reaction probabilities  $P_{\alpha j l \alpha' j' l'}^{JPS}$  for all  $j, j', l$ , and  $l'$  values and for  $\alpha' = 2$  and  $3$  with  $\alpha = 1$ :

$$N_{\nu\nu'}^{JPS}(E) = \sum_{\alpha'=2,3} \sum_{j'l'} P_{\alpha\nu j|\alpha'\nu'j'l'}^{JPS} \quad (5)$$

The vibrationally specific DORS is obtained by an analytic derivative of a cubic spline fit to the vibrationally specific reaction probability,  $\rho_{\nu\nu'}^{JPS}(E)$ .

$$\rho_{\nu\nu'}^{JPS}(E) = \frac{d}{dE} N_{\nu\nu'}^{JPS}(E) \quad (6)$$

In a similar fashion we can sum either over all initial states or over all final states for a specific final or initial state to obtain reaction probabilities ( $N_n^{JPS}$  or  $N_{n'}^{JPS}$ ) and the corresponding DORS ( $\rho_{n'}^{JPS}$  or  $\rho_n^{JPS}$ ) that are final- or initial-state-specific, respectively.

### III. Results

We present the results for the various  $JPS$  values below. The parity,  $P$ , is defined as  $P = (-1)^{j+l}$  which always gives a +1 parity for  $J = 0$  ( $j = l$ ), and two parities [+1 (even) and -1 (odd)] for  $J > 0$ . The spatial permutation symmetry term  $S$  may be defined for atom-diatom reactions such as  $\text{X} + \text{H}_2 \rightarrow \text{XH} + \text{H}$  and is related to the nuclear spin function.  $S = +1$  for *para* hydrogen and -1 for *ortho* hydrogen. All the results presented below have  $S = +1$ .

**$JPS = 0++$ .** Figure 1 shows the accurate quantal CRP,  $N^{JPS}(E)$ , as squares, for  $JPS = 0++$ . A spline fit to the CRP data (which is shown as the solid line in Figure 1) is then analytically differentiated to obtain the first derivative of the CRP with respect to energy, i.e., the DORS curve. This is shown as the dashed line in Figure 1. We see seven features, namely, six peaks and a shoulder. We will use the method outlined above where we fit the DORS curve to a sum of line shape functions defined by eq 4. We treat  $W_\gamma$ ,  $E_\gamma$ , and  $\kappa_\gamma$  as adjustable parameters in our fit. We can reproduce the curve quite accurately by using a sum of nine terms. The line shape curves, their sum, and the DORS curve are shown in Figure 2. The nine individual bell-shaped curves are shown as dotted lines and their sum as squares. The sum is seen to be an excellent fit to the solid line, which is the DORS plot, obtained from the quantum calculations. Each of the line shape functions corresponds to a transition state and may be assigned a label consisting of the quantum numbers  $[\nu_1\nu_2^K]$ . The value of the energy (at the maximum, unless specifically stated to be at a different place) of each feature or the  $E_{\text{max}}$  value, the assignments, the semiclassical energies from the VA curves, and the fit parameters for each of the line shape functions are shown in Table 1. The root-mean-square (RMS) error of the fit over the energy range 0.32–1.1 eV is 0.14 eV<sup>-1</sup>. The assignments are explained in detail below. The semiclassical energy of the VA curve corresponds to the energy of the dynamical bottleneck, which, for nonstretch excited states, is the highest point on the curve on either the product side or the reactant side of the reaction coordinate. For stretch-excited states, we choose the maximum of the curve that is not in the region of high reaction-path curvature. The semiclassical energy of the supernumerary state is the energy at the maximum of the VA curve in the product side of the reaction coordinate, again away from the region of high reaction-path curvature. We note that transition state theory assumes that all the  $\kappa_\gamma$  for each transition state are unity. Several of the values of the transmission coefficients, however, differ from this ideal. This could be a result of the approximations made regarding parabolic effective energy barriers or the fact that the state is not an ideal dynamical bottleneck.

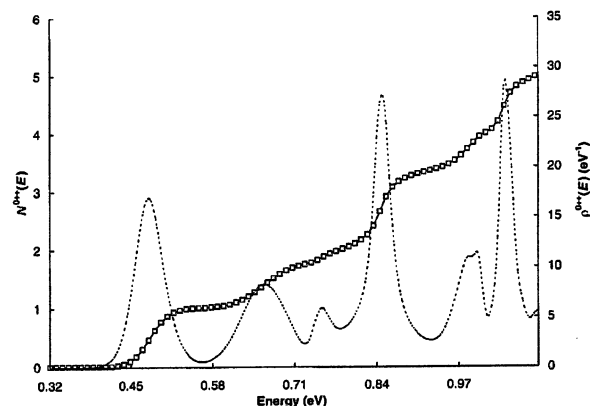


**Figure 1.** Accurate quantal cumulative reaction probability for  $JPS = 0++$  (squares), spline fit to the CRP (solid line), and density of reactive states (dashed line) as functions of the energy for  $JPS = 0++$ .

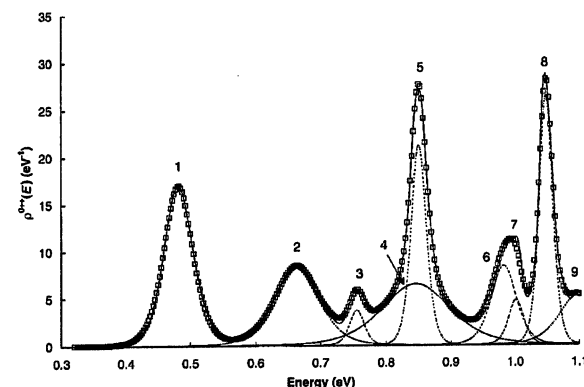


**Figure 2.** Line shape functions (dashed lines), their sum (solid line), and the density of reactive states (squares) as a function of the energy for  $JPS = 0++$ .

**TABLE 1:  $E_{\text{max}}$  Values for the Features in the DORS Curves, the Transition State Assignments, the Semiclassical Energies from the VA Curves, and the Fit Parameters for  $JPS = 0++$**

feature	$E_{\text{max}}$ (eV) (DORS)	$[\nu_1\nu_2^K]$	semiclassical energy (eV)	$W_\gamma$	$E_\gamma$ (eV)	$\kappa_\gamma$
1	0.481	[00 <sup>0</sup> ]	0.511	0.015	0.482	1.01
2	0.664	[02 <sup>0</sup> ]	0.757	0.023	0.663	0.75
3	0.756	[s10 <sup>0</sup> ]	0.729	0.008	0.755	0.11
4	0.851	[04 <sup>0</sup> ]	1.071	0.035	0.847	0.91
5	0.851	[10 <sup>0</sup> ]	0.846	0.008	0.851	0.66
6	0.991	[12 <sup>0</sup> ]	1.028	0.013	0.982	0.43
7	1.000	[06 <sup>0</sup> ]	1.426	0.008	1.001	0.15
8	1.048	[s20 <sup>0</sup> ]	1.037	0.007	1.048	0.74
9	1.100 <sup>a</sup>	na <sup>b</sup>		0.020	1.098	0.42

<sup>a</sup> The CRP data end at 1.1 eV. <sup>b</sup> This feature was not assigned (see text).

The VA curves for  $J = 0$  are shown in Figure 3a–c. They are also labeled by  $[\nu_1\nu_2^K]$ . Since the bends are treated by a quadratic-quartic fit to the bending potential, the semiclassical energy thresholds obtained for high  $\nu_2$  states are not expected to be quantitatively accurate. The energies of the low  $\nu_1$  and  $\nu_2$  states should, however, correlate well with the quantized thresholds for the same states.

Feature 1 is easily assigned to the [00<sup>0</sup>] state, as it is the overall reaction threshold. Feature 2 is assigned to the [02<sup>0</sup>] state since only even bend states are allowed for  $J = 0$ . (This is because  $K \leq J$  and  $K = \nu_2, \nu_2 - 2, \dots, 0$  or 1). Furthermore,

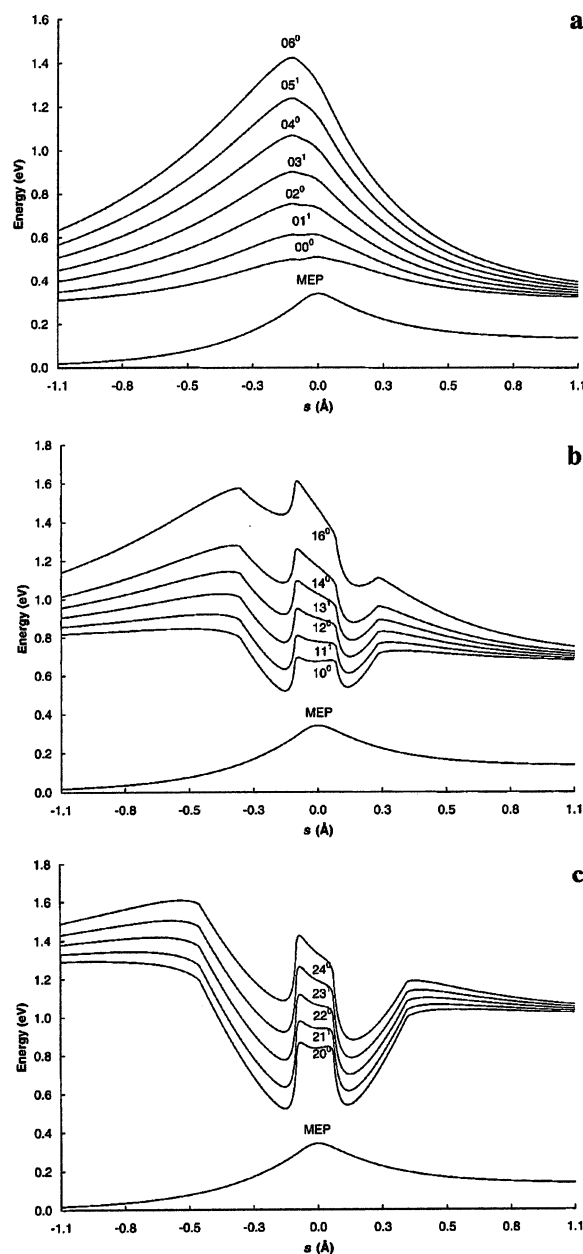


**Figure 3.** Vibrational adiabatic curves in increasing order from the second-lowest curve for (a)  $[00^0]$ ,  $[01^1]$ ,  $[02^0]$ ,  $[03^1]$ ,  $[04^0]$ ,  $[05^1]$ ,  $[06^0]$ , (b)  $[10^0]$ ,  $[11^1]$ ,  $[12^0]$ ,  $[13^1]$ ,  $[14^0]$ ,  $[16^0]$ , and (c)  $[20^0]$ ,  $[21^1]$ ,  $[22^0]$ . The lowest curve in each panel shows the  $V_{\text{MEP}}$  as a function of the distance from the saddle point.

the energy of the second feature is well below the semiclassical energy threshold for states with  $\nu_1 = 1$ . Feature 3 appears at too low an energy to be the variational transition state  $[10^0]$ . It is, however, located very close to the semiclassical energy threshold of the product-like  $[10^0]$  vibrational adiabatic state (0.76 eV for feature 3 versus 0.73 eV for the semiclassical threshold from the VA curve). We therefore assign feature 3 to the supernumerary state  $[s10^0]$ . Supernumerary transition states have been identified earlier for other reactions.<sup>5,15</sup> They may be considered as dynamical bottlenecks in the product channel. Supernumerary transition states have been classified into those of the first kind (which influence total reactivity) and those of

the second kind (which influence only state-to-state reactivity). As feature 3 clearly influences the total reactivity we classify it as a supernumerary state of the first kind. Supernumeraries of the second kind can be identified by looking at state-specific spectra.

Figures 4a,b and 5a,b show the state-specific spectra for various initial and final conditions. Parts a and b of Figure 4 show the state-to-state DORS curves for various initial  $\nu$  and final  $\nu'$  values summed over the  $j$  and  $j'$  values. Parts a and b of Figure 5 show the state-to-state DORS curves for various individual initial ( $\nu, j$ ) and final ( $\nu', j'$ ) channels. To use the state-specific spectra to assign the stretch and bend quantum numbers, we first note that, to the extent that a transition may be considered vibrationally adiabatic, the stretch quantum numbers,  $\nu_1$ , have a propensity to correlate to the diatomic vibrational quantum number  $\nu$ .<sup>3,41</sup> This is called<sup>3</sup> half-collision stretch adiabaticity. A vibrationally nonadiabatic traversal of the path to the transition state leads to  $\nu \neq \nu_1$ .

Figure 4a shows the state-to-state DORS curve for  $\rho_{0 \rightarrow 0}^{0++}$ . The first two maxima of the curve correspond to features 1 and 2. This confirms our assignment of the features as  $[00^0]$  and  $[02^0]$ , respectively. Since  $\nu = \nu_1$ , these two transition states are vibrationally adiabatic transition states. The state-specific DORS plot for all channels with initial  $\nu = 0$  summed over all  $j$  and for all final channels with  $\nu' = 1$  summed over all  $j'$  is also shown in Figure 4a. The first peak at ca. 0.73 eV indicates the onset of flux into the product  $\nu' = 1$  channel. This confirms our assignment of feature 3 as the supernumerary state  $[s10^0]$ .

As noted earlier, comparisons with the semiclassical energy thresholds from the VA curves become less useful in cases where the bend is highly excited (i.e.,  $\nu_2 \geq 2$ ). We must, therefore, use other methods to assign quantum numbers to the high  $\nu_2$  states. One of these is the energetic separation of the states differing in only the bend quantum numbers in a given  $\nu_1$  manifold. We can expect the energy separations of the  $[0\nu_2^0]$  states to be an approximately linear function of  $\nu_2$ , at least for small  $\nu_2$ .<sup>2</sup> On this basis, since the energy separation between the maximum of feature 1 ( $[00^0]$ ) and feature 2 ( $[02^0]$ ) is 0.18 eV, and since the feature that is separated by about 0.18 eV from the maximum of feature 2 is feature 4, we may assign feature 4 to the  $[04^0]$  state. Feature 4 is also broader than features 1 or 2 and this is in keeping with the tendency for the peaks within a given  $\nu_1$  manifold to both broaden and shorten as  $\nu_2$  increases.<sup>5</sup> This tendency can be understood by looking at the VA curves for a given  $\nu_1$ . Figure 3b shows the VA curves for  $[\nu_1 = 1, \nu_2 = 0, 1, 2^{K=0 \text{ or } 1}]$ . We see that as  $\nu_2$  increases the peaks corresponding to the dynamical bottlenecks become narrower, thus facilitating greater tunneling. In relation to the CRP curve this means that the sharp "steps" in the reaction probability become smoothed out, which translates to broadening of the peaks in the DORS curve.

The state-specific DORS curve for initial  $\nu = 0$  and  $j = 0, 2, 4, 6$ , and 8 channels summed over all final channels is shown in Figure 5a. Flux from the (0,0) and (0,2) channels peaks strongly at the energy of feature 1 (the  $[00^0]$  threshold) and less strongly at that of feature 2 (the  $[02^0]$  threshold). The (0,4) channel, however, couples strongly to the  $[02^0]$  threshold but hardly couples at all to the  $[00^0]$  threshold. The reason for this is understood if we compare the threshold energy for the  $[00^0]$  state, which is 0.482 eV, to the asymptotic energies of the (0,0), (0,2), and (0,4) channels which are 0.268, 0.312, and 0.414 eV, respectively. The difference between the threshold energy and the asymptotic energy is 0.214, 0.170, and 0.068 eV for the (0,0), (0,2), and (0,4) channels, respectively. The (0,4) channel

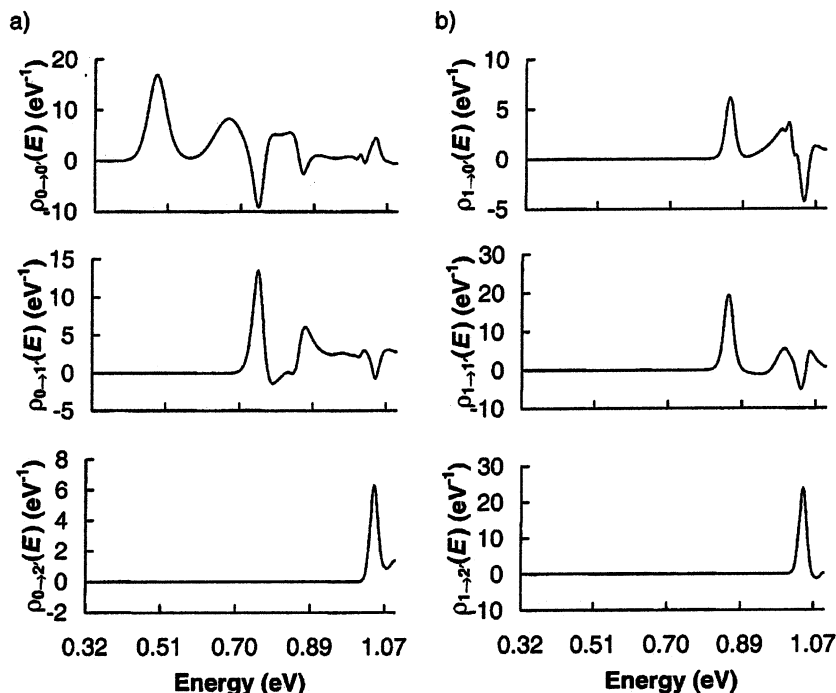


**Figure 4.** State-specific spectra for (a) initial  $v = 0$  and final  $v' = 0, 1$ , and  $2$  summed over all initial and final  $j$  and (b) initial  $v = 1$  and final  $v' = 0, 1$ , and  $2$  summed over all initial and final  $j$ . All panels are for  $JPS = 0++$ .

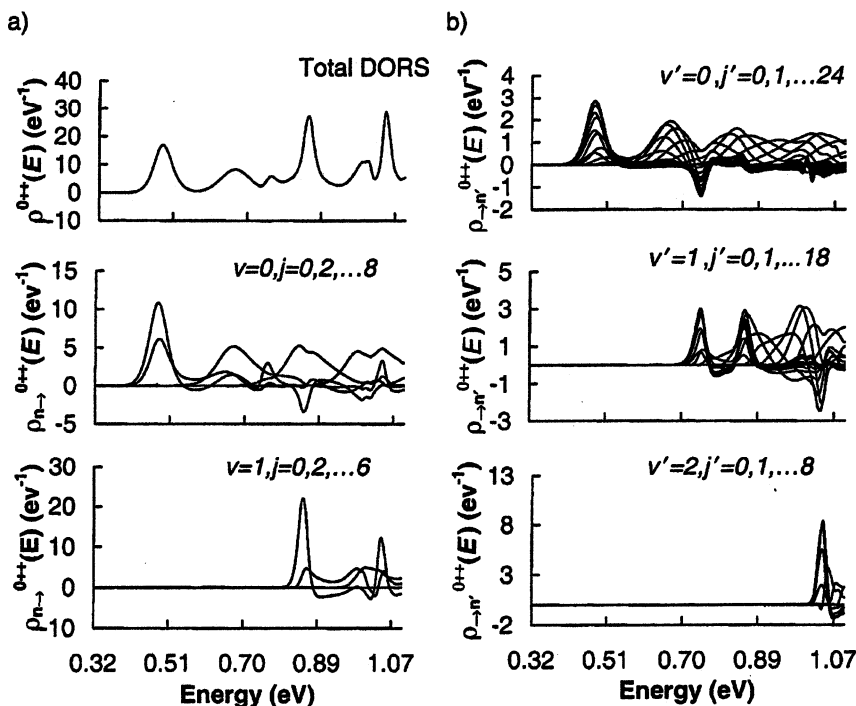


**Figure 5.** (a) State-specific spectra for initial  $v = 0, j = 0, 2, \dots, 8$  and  $v = 1, j = 0, 2, \dots, 6$ . The topmost panel shows the total density of reactive states for comparison. (b) State-specific spectra for final  $v' = 0, j' = 0, 1, \dots, 24$ ,  $v' = 1, j' = 0, 1, \dots, 18$ , and  $v' = 2, j' = 0, 1, \dots, 8$ . All panels are for  $JPS = 0++$ .

is, therefore, energetically accessible, and as in the  $\text{H} + \text{H}_2$  reaction,<sup>3</sup> we conclude that the reason that the channel does not couple to the  $[00^0]$  threshold is not because the dynamics of the reaction prevent it from doing so, but because of the nature of the PES. The fact that the  $(0,4)$  channel does not couple to the  $[00^0]$  state is also a specific example of a more general

correlation between the rotational quantum number of the diatomic and the bend quantum number of the transition state. We discuss this in more detail in section IV. The  $(0,6)$  channel couples to the  $[04^0]$  threshold. Thus we see that all these transition states display good stretch adiabaticity. Figure 5a also shows the state-selected DORS curve for initial  $v = 1$  and  $j =$

0, 2, 4, and 6 channels summed over all final channels. The trends are similar to those described above. The (1,0) DORS curve shows a very strong maximum at the energy of feature 5. We also find that the semiclassical energy of the  $[10^0]$  state is within 5 meV of the maximum of feature 5. On the basis of the above evidence, we assign feature 5 to the  $[10^0]$  state. The VA curves indicate that those states for which the stretch is not excited ( $\nu_1 = 0$ ) allow for greater tunneling than those for which stretch excitation is present. This is borne out by feature 5, which is tall and thin compared to the non-stretch-excited states.

We assign feature 6 to the state  $[12^0]$ , mainly by looking at the state-specific DORS curves. Comparison to the semiclassical energy is inconclusive, as the state is bend-excited. Figure 4b shows the state-specific DORS curve for initial  $\nu = 1$  and final  $\nu' = 1$  summed over all initial and final  $j$ . The curve has its first maximum at the threshold of  $[10^0]$  and a second maximum close to the energy of feature 6. Figure 5b shows that both the initial (1,2) channel and the (1,4) channel have considerable flux close to the peak of feature 6. Thus, like the  $[10^0]$  state, the  $[12^0]$  state is also vibrationally adiabatic.

Feature 7 is assigned to be the  $[06^0]$  state since the initial (0,8) channel displays considerable flux at the maximum of feature 7. Figure 5a shows that the difference between the energy at the maximum of the (0,6) DORS curve and the (0,8) DORS curve is about 0.15 eV. The difference in the energy at the maximum of feature 7 and the energy at the maximum of feature 4 is also 0.15 eV, and this is only slightly smaller than the spacing between the  $[00^0]$  and the  $[02^0]$  states and the  $[02^0]$  and the  $[04^0]$  states.

Features 8 and 9 overlap substantially. Only part of feature 9 is seen, since the quantum results are not available beyond 1.1 eV. It is not possible to assign feature 9 unambiguously. Due to the substantial overlap with feature 9, the assignment of feature 8 is only provisional. Feature 8 is very close to the semiclassical threshold energy for the product side  $[20^0]$  state, differing from it by only 0.01 eV. The state-specific DORS curve for the final  $\nu' = 2$  summed over all  $j'$  is shown in Figure 5b. The curve shows a maximum at the energy of the maximum of feature 8. The initial  $\nu = 2$  threshold is not energetically accessible, which implies that the feature is too low in energy to be the  $[20^0]$  state. Thus, we assign the feature to be, at least in part, due to the  $[s20^0]$  state. A more definitive assignment cannot be made until the CRP data for higher energies is available.

**$JPS = 1++$ .** The spectrum for  $JPS = 1++$  will contain those features that have  $K = 1$  and for which  $\nu_2$  is an odd number. The accurate quantal CRP data (squares) as well as the spline fit to the data (solid line) are shown in Figure 6. The DORS curve, obtained by an analytic first derivative of the spline fit is shown as the dashed line in Figure 6. We fit the DORS curve using a sum of line shape functions as we did for the  $JPS = 0++$  data. The curve is well approximated to plotting accuracy by using a sum of six line shape functions. The line shape functions, their sum, and the DORS curve are shown in Figure 7. We make assignments to the features in the DORS curve in terms of  $[\nu_1\nu_2^K]$  as before, using methods similar to the ones described above for the  $JPS = 0++$  spectrum. Table 2 shows the  $E_{\max}$  value of each feature, the assignments, the semiclassical energies from the VA curves, and the fit parameters for each of the transition states. The RMS error of the fit over the energy range 0.32–1.1 eV is 0.13 eV<sup>-1</sup>. As the total angular momentum  $J$  changes, the semiclassical energy of the dynamical bottleneck also changes by approximately  $BJ(J+1)$  where  $B$  is the rotational constant of the system at the geometry of the dynamical bottleneck. For the  $\text{ClH}_2$  system the rotational constant at the

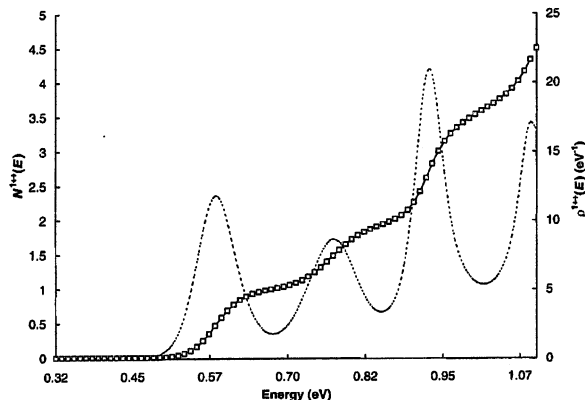


**Figure 6.** Accurate quantal CRP (squares), spline fit to the CRP (solid line), and density of reactive states (dashed line) as functions of the energy for  $JPS = 1++$ .

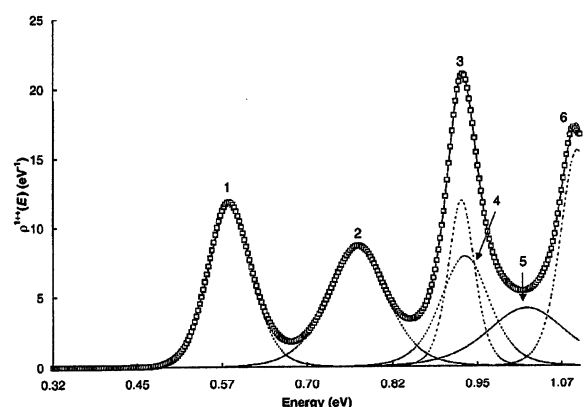


**Figure 7.** Line shape functions (dashed lines), their sum (solid line), and the density of reactive states (squares) as a function of the energy for  $JPS = 1++$ .

**TABLE 2:  $E_{\max}$  Values for the Features in the DORS Curves, the Transition State Assignments, the Semiclassical Energies from the VA Curves, and the Fit Parameters for  $JPS = 1++$**

feature	$E_{\max}$ (eV) (DORS)	semiclassical energy <sup>a</sup> (eV) $[\nu_1\nu_2^K]$	$W_\gamma$	$E_\gamma$ (eV)	$\kappa_\gamma$
1	0.580	0.617	0.021	0.581	0.99
2	0.769	0.905	0.029	0.768	0.97
3	0.923	0.922	0.013	0.921	0.61
4	0.923	1.241	0.024	0.926	0.75
5	1.012 <sup>b</sup>	0.892	0.039	1.019	0.64
6	1.090	1.144	0.016	1.093	1.02

<sup>a</sup> This is the semiclassical energy for  $J = 0$ . <sup>b</sup> This is the energy at the minimum of the DORS curve just before feature 6.

dynamical bottlenecks, up to at least 1 Å away from the saddle point, along the reaction path is of the order of  $2 \times 10^{-4}$  eV. Thus, for  $J = 1$ , the change in the semiclassical energies from the  $J = 0$  values, at the dynamical bottlenecks, is of the order of  $4 \times 10^{-4}$  eV. For the purposes of comparing the semiclassical energy of a transition state to the estimate of the energy from the DORS curve for  $J = 1$ , we therefore use the semiclassical energies of the  $J = 0$  curves and the semiclassical energies listed in Table 2 are the ones for  $J = 0$ .

Since the  $JPS = 1++$  DORS plot contains features only with odd  $\nu_2$  values, the first feature is easily assigned to be  $[01^1]$ . The validity of this assignment is borne out by comparing the energy of the maximum of the first feature, i.e., the  $E_{\max}$  value

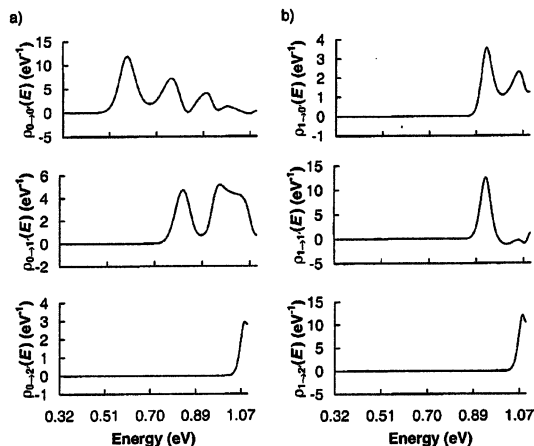


**Figure 8.** State-specific spectra for (a) initial  $\nu = 0$  and final  $\nu' = 0, 1$ , and  $2$  summed over all initial and final  $j$  and (b) initial  $\nu = 1$  and final  $\nu' = 0, 1$ , and  $2$  summed over all initial and final  $j$ . All panels are for  $JPS = 1++$ .

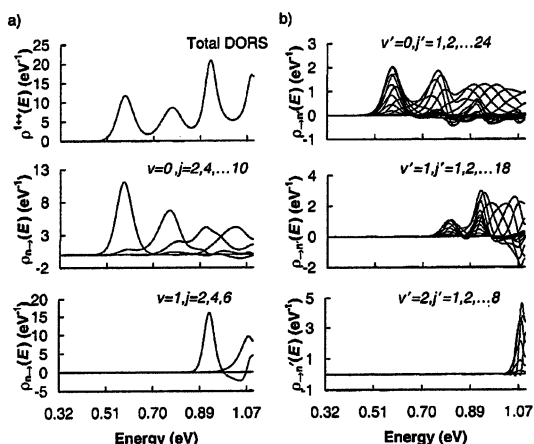


**Figure 9.** (a) State-specific spectra for initial  $\nu = 0, j = 2, 4, \dots, 10$  and  $\nu = 1, j = 2, 4, 6$ . The topmost panel shows the total density of reactive states for comparison. (b) State-specific spectra for final  $\nu' = 0, j' = 1, 2, \dots, 24$ ,  $\nu' = 1, j' = 1, 2, \dots, 18$ , and  $\nu' = 2, j' = 1, 2, \dots, 8$ . All panels are for  $JPS = 1++$ .

of the first feature, to the semiclassical energy. The values differ only by 0.04 eV. Parts a and b of Figure 8 show the state-specific DORS curves for various values of initial and final  $\nu$  quantum numbers summed over all initial and final  $j$ . Parts a and b of Figure 9 show the individual state-specific DORS curves for various values of initial and final  $\nu$  and  $j$  quantum numbers.

The state-specific DORS curve with initial  $\nu = 0$  and  $\nu' = 0$ , summed over all  $j$  and  $j'$  shows a maximum at the energy of the maximum of feature 1. Similar to the assignment of feature 1, we assign the second peak to  $[03^1]$  also on the basis of the state-specific spectra. The semiclassical energy comparison is unreliable at such high levels of bend excitation. As in the  $JPS = 0++$  spectrum, both the features are due to stretch adiabatic transitions.

The third feature is a tall peak that has a small width, indicative, as in the  $J = 0$  spectrum, of the onset of the stretch excitations. We have assigned the third feature to the  $[11^1]$  level, based on evidence from the state-specific DORS curves as well as by comparisons to the semiclassical energy from the VA curve. The state-specific DORS curves for  $\nu = 1$  and  $\nu' = 0$

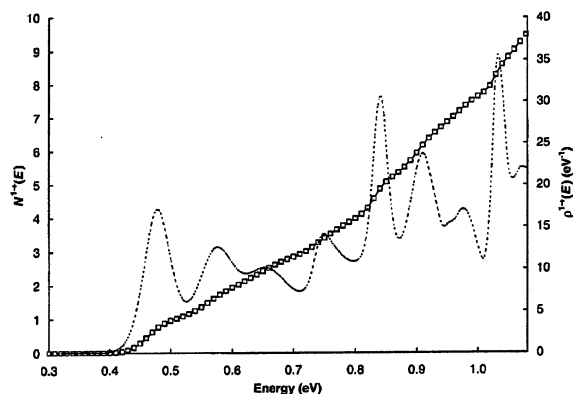


**Figure 10.** Accurate quantal CRP (squares), spline fit to the CRP (solid line), and density of reactive states (dashed line) as functions of the energy for  $JPS = 1-+-$ .

and 1 summed over all  $j$  and  $j'$  shows the onset of flux in the  $\nu = 1$  channel at the energy of the maximum of the third feature.

The fourth peak is assigned to be  $[05^1]$ , again, on the basis of evidence from the state-specific DORS curves. The difference in the  $E_{\nu}$  values between the  $[01^1]$  and the  $[03^1]$  states is about 0.18 eV, and that between the  $[03^1]$  state and the fourth feature, about 0.16 eV. As for  $J = 0$ , we expect that the differences between the energies of the states for successive  $\nu_2$  values at a given value of  $\nu_1$  will be approximately constant.

The fifth feature may be assigned, in part, to the  $[07^1]$  state. The state-specific curves for initial  $\nu = 0$  and various  $j$  summed over all final quantum numbers is shown in Figure 9a. The sequence of peaks indicates the progression of  $\nu_2$  values within the  $\nu_1 = 0$  manifold. The feature is, however, anomalously close to the  $[05^1]$  state in energy. The reason for this is unclear. It is possible that the fit distorts the true position of the state due to the strong overlap of feature 5 with its neighboring features (one of them an ill-defined feature 6).

The sixth feature is incomplete since we did not perform the quantum calculations beyond 1.1 eV. A provisional assignment, based on the state-specific spectra is the state  $[13^1]$ . The DORS curve for initial  $\nu = 1$  and final  $\nu' = 2$ , summed over  $j$  and  $j'$ , shows a peak at the energy of this feature. The finding of considerable flux in the initial  $\nu = 1$  channel, the fact that the feature is tall with a small width, and the location of the position of the maximum of the feature in relation to the  $E_{\text{max}}$  of the  $[11^1]$  peak all indicate a stretch-excited feature. For future study it would be interesting to calculate CRP data at higher energies to help confirm the assignment.

**$JPS = 1-+-$ .** The accurate quantal CRP for  $JPS = 1-+-$ , the spline fit to the data, and the DORS curve are shown in Figure 10. The DORS curve is fit as before, with the fit requiring a sum of 13 line shape functions. Figure 11 shows the line shape functions, their sum, and the DORS curve. The DORS curve for  $JPS = 1-+-$  contains features with both even and odd values of  $\nu_2$  and  $K$  values of both 0 and 1. Consequently, the features of the  $JPS = 1++$  spectrum should be duplicated in the  $JPS = 1-+-$  spectrum and the features corresponding to the  $JPS = 1++$  spectrum may be assigned using the previous,  $JPS = 1++$ , assignments. The remaining features correspond to even  $\nu_2$  values. The even bend states will occur in positions close to where they occurred in the  $JPS = 0++$  spectrum. All the  $E_{\text{max}}$  values, the assignments, the semiclassical energies from the ( $J = 0$ ) VA curves, and the fit parameters for each of the transition states are shown in Table 3. The RMS error of the fit in the range 0.32–1.1 eV is 0.14  $\text{eV}^{-1}$ .



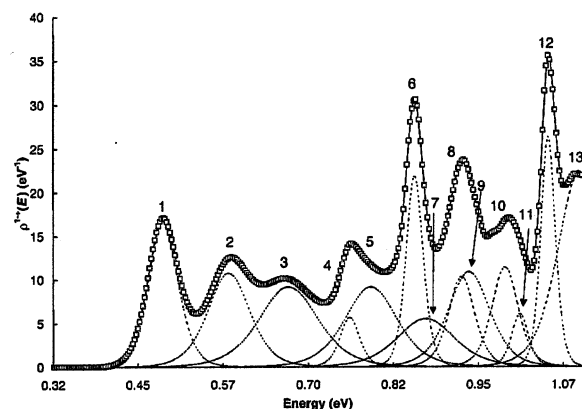


**Figure 11.** Line shape functions (dashed lines), their sum (solid line), and the density of reactive states (squares) as a function of the energy for  $JPS = 1-+$ .

**TABLE 3:  $E_{\text{max}}$  Values for the Features in the DORS Curves, the Transition State Assignments, the Semiclassical Energies from the VA Curves, and the Fit Parameters for  $JPS = 1-+$**

feature	$E_{\text{max}}$ (eV) (DORS)	$[\nu_1\nu_2K]$	semiclassical energy <sup>a</sup> (eV)	$W_\gamma$	$E_\gamma$ (eV)	$\kappa_\gamma$
1	0.482	[00 <sup>0</sup> ]	0.511	0.015	0.482	0.98
2	0.583	[01 <sup>1</sup> ]	0.617	0.021	0.578	0.89
3	0.660	[02 <sup>0</sup> ]	0.757	0.029	0.666	1.06
4	0.760	[s10 <sup>0</sup> ]	0.729	0.010	0.756	0.22
5	0.806 <sup>b</sup>	[03 <sup>1</sup> ]	0.905	0.026	0.787	0.94
6	0.851	[10 <sup>0</sup> ]	0.846	0.008	0.851	0.73
7	0.851	[04 <sup>0</sup> ]	1.071	0.028	0.868	0.62
8	0.922	[11 <sup>1</sup> ]	0.922	0.013	0.920	0.54
9	0.922	[05 <sup>1</sup> ]	1.241	0.021	0.931	0.89
10	0.989	[12 <sup>0</sup> ]	1.028	0.013	0.984	0.59
11	0.989	[06 <sup>0</sup> ] <sup>c</sup>	1.426	0.008	1.006	0.20
12	1.049	[s20 <sup>0</sup> ] <sup>c</sup>	1.037	0.007	1.048	0.75
13	1.091	[13 <sup>1</sup> ]	1.144	0.021	1.094	1.88

<sup>a</sup> This is the semiclassical energy for  $J = 0$ . <sup>b</sup> This is at the minimum of the DORS curve just before feature 6. <sup>c</sup> The feature may include the [07<sup>1</sup>] state unresolved due to overlap (see text).

Features 1, 2, and 3 are easily assigned to the states [00<sup>0</sup>], [01<sup>1</sup>], and [02<sup>0</sup>], respectively. Feature 1 is the overall reaction threshold and the assignments for features 2 and 3 follow from the assignments in the spectra of  $JPS = 0++$  and  $JPS = 1++$ . The semiclassical energies comparisons are valid for small bend excitations such as  $\nu_2 = 1$  and comparing the semiclassical energy for the [01<sup>1</sup>] state to the  $E_{\text{max}}$  for feature 2 shows that they differ by only about 0.03 eV.

Feature 4 is assigned to be the supernumerary [s10<sup>0</sup>] state on the basis of the comparison with the semiclassical energy. The feature occurs close to the same energy in the spectrum as it does in the  $J = 0$  spectrum. The state-specific spectra for various values of initial ( $\nu, j$ ) and final ( $\nu', j'$ ) are shown in Figures 12a,b and 13a,b. The spectra for the states with initial  $\nu = 0$  and final  $\nu' = 1$  show the threshold for flux into the final  $\nu' = 1$  state at the energy of feature 4.

Feature 5 is assigned to the [03<sup>1</sup>] state on the basis of the  $JPS = 1++$  assignment as well as the state-specific DORS curve of the  $\nu = 0, \nu' = 0$  states. The DORS curve shows a maximum at the energy of feature 5, which indicates flux out of the  $\nu = 0$  and into the  $\nu' = 0$  state. Thus, this is also a stretch adiabatic feature.

The  $\nu = 1, \nu' = 1$  DORS curve in Figure 12b shows the threshold for flux into the product  $\nu' = 1$  channels at the energy of the sixth feature. We therefore assign the sixth feature as the

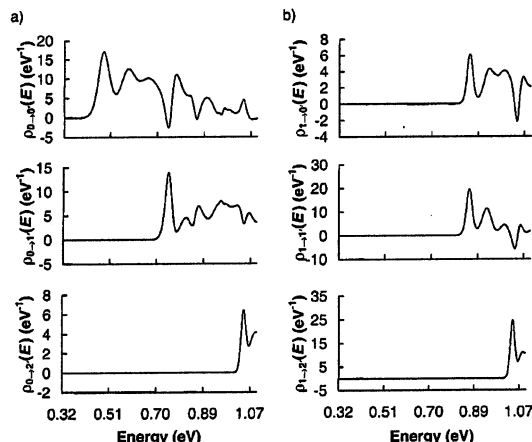


**Figure 12.** State-specific spectra for (a) initial  $\nu = 0$  and final  $\nu' = 0, 1$ , and 2 summed over all initial and final  $j$  and (b) initial  $\nu = 1$  and final  $\nu' = 0, 1$ , and 2 summed over all initial and final  $j$ . All panels are for  $JPS = 1-+$ .

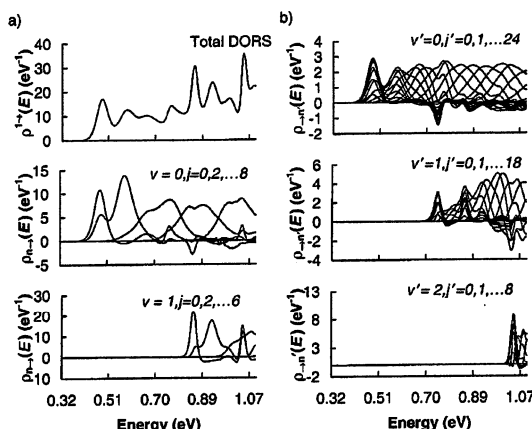


**Figure 13.** (a) State-specific spectra for initial  $\nu = 0, j = 0, 2, \dots, 8$  and  $\nu = 1, j = 0, 2, \dots, 6$ . The topmost panel shows the total density of reactive states for comparison. (b) State-specific spectra for final  $\nu' = 0, j' = 0, 1, \dots, 24$ ,  $\nu' = 1, j' = 0, 1, \dots, 18$ , and  $\nu' = 2, j' = 0, 1, \dots, 8$ . All panels are for  $JPS = 1-+$ .

stretch adiabatic state [10<sup>0</sup>]. Analogous to the corresponding feature in the  $JPS = 0++$  spectrum we assign feature 7 as the [04<sup>0</sup>] state. Both state-specific DORS curves as well as the progression of the  $E_\gamma$  values for successive bend excitations in the  $\nu_1 = 0$  manifold confirm the assignment. Following the assignments in the spectra of  $JPS = 1++$  we assign features 8 and 9 to the states [11<sup>1</sup>] and [05<sup>1</sup>], respectively.

Features 10 and 11 correspond to the states [12<sup>0</sup>] and [06<sup>0</sup>], respectively. The assignment is confirmed by the state-specific DORS curves as well as the assignments of the  $JPS = 0++$  spectrum. Feature 12 is the supernumerary [s20<sup>0</sup>] state, indicated by both a comparison with the semiclassical energy as well as by the state-specific DORS curve, which shows flux into the final  $\nu' = 2$  state. The feature also probably includes the [07<sup>1</sup>] state, which is seen in the  $JPS = 1++$  spectrum. The higher density of states of the  $1-+$  spectrum and the resulting overlap of features leads to the obscuring of some features that are present in the "cleaner",  $1++$ , spectrum.

The 13th, final, feature is ill defined and incomplete due to the lack of CRP data at higher energies. We provisionally assign this feature to the [13<sup>1</sup>] state on the basis of the assignment made in the  $JPS = 1++$  spectrum as well by looking at the

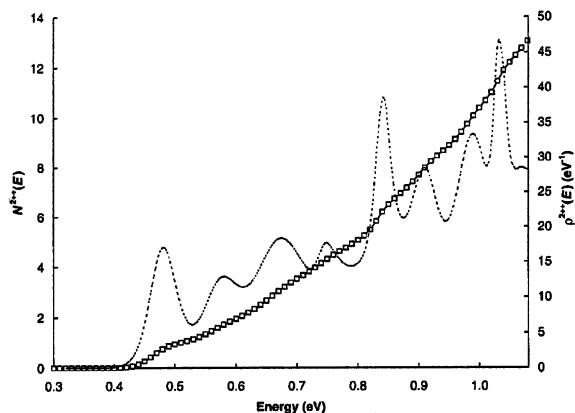


**Figure 14.** Accurate quantal CRP (squares), spline fit to the CRP (solid line), and density of reactive states (dashed line) as functions of the energy for  $JPS = 2++$ .

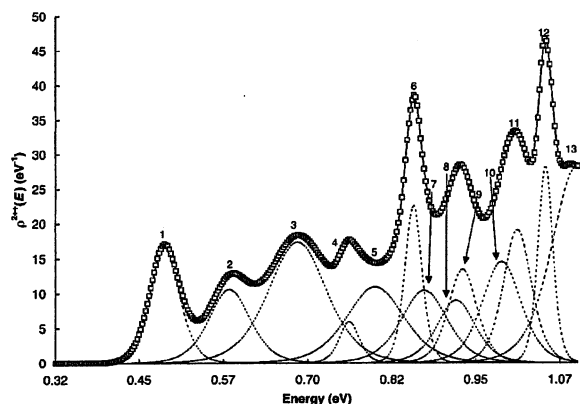


**Figure 15.** Line shape functions (dashed lines), their sum (solid line), and the density of reactive states (squares) as functions of the energy for  $JPS = 2++$ .

state-specific DORS curves for channels with initial  $v = 1$ , which show flux around the  $E_{\text{max}}$  of feature 13.

**$JPS = 2++$ .** The CRP data for  $JPS = 2++$  is shown, along with a spline fit to the data, in Figure 14. The spline fit is analytically differentiated to give the DORS curve also shown in Figure 14, as the dashed line. We fit the DORS curve, as before, using a sum of line shape functions. We can reproduce the curve quite well using 13 line shape functions. The line

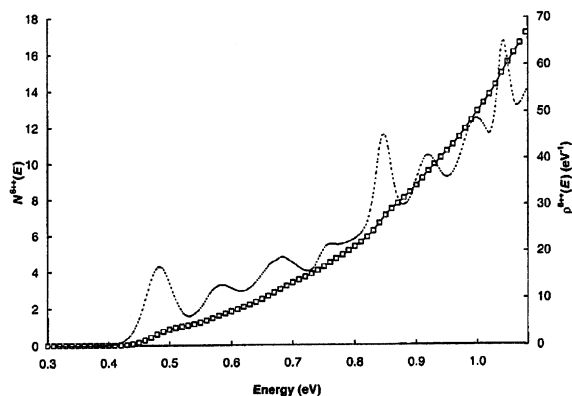


**Figure 16.** Accurate quantal CRP (squares), spline fit to the CRP (solid line), and density of reactive states (dashed line) as functions of the energy for  $JPS = 6++$ .

shape functions are shown in Figure 15. We assigned quantum numbers  $[\nu_1\nu_2^K]$  to the features of the DORS curve using the assignments we made for the  $JPS = 0++$ ,  $1++$ , and  $1-+$  spectra as our guide. The  $E_{\text{max}}$  value of each feature, the assignments, and the fit parameters for the 13 transition states are presented in Table 4. The RMS error of the fit over the range 0.32–1.1 eV is 0.12 eV<sup>-1</sup>.

We note that several of the  $\kappa_\gamma$  values are greater than 1. As discussed in section II, this is because for  $J = 2$ ,  $K = 0$  and 2 for the even bend states and 1 for the odd bend states. Further, states for which  $K > 0$  are doubly degenerate. Thus, the third feature contains both the  $[02^0]$  and one of the  $[02^2]$  states and is designated as  $[02^{0,2}]$ . The  $JPS = 2-+$  spectrum (which is not shown) contains the other  $[02^2]$  state. Table 4 lists the degeneracies of each level as well as the running sum of the degeneracies. We note that the running sum of the degeneracies up to a particular state approximately corresponds to the value of the CRP at the  $E_\gamma$  of that state, almost up to 1 eV. The different  $K$  values are not resolved since the separation for states differing only in  $K$  values is small compared to the separation between states differing in bend and stretch quantum numbers.<sup>5</sup> Thus, we find that the  $\kappa_\gamma$  values for bend states with  $\nu_2 \geq 2$  are greater than 1, indicating the presence of other, unresolved states differing only in the value of  $K$ . This is seen in features 3, 5, 7, 10, and 11.

**$JPS = 6++$ .** Figure 16 shows the CRP data for  $JPS = 6++$ , the spline fit to the data, and the DORS curve obtained by differentiating the spline fit analytically. We fit the DORS curve

**TABLE 4:**  $E_{\text{max}}$  Values for the Features in the DORS Curves, the Transition State Assignments, the Fit Parameters, the Degeneracy of Each Transition State, and the Running Sum of Degeneracies for  $JPS = 2++$

feature	$E_{\text{max}}$ (eV) (DORS)	$[\nu_1\nu_2^K]$	$W_\gamma$	$E_\gamma$ (eV)	$\kappa_\gamma$	degeneracy <sup>a</sup>	running sum
1	0.483	$[00^0]$	0.015	0.483	0.98	1	1
2	0.586	$[01^1]$	0.021	0.579	0.87	1	2
3	0.682	$[02^{0,2}]$	0.029	0.680	2.01	1,1	4
4	0.758	$[s10^0]$	0.010	0.757	0.24		4
5	0.798 <sup>b</sup>	$[03^1]$	0.029	0.796	1.26	1	5
6	0.853	$[10^0]$	0.009	0.852	0.77	1	6
7	0.853	$[04^{0,2}]$	0.023	0.868	0.96	1,1	8
8	0.922	$[11^1]$	0.020	0.916	0.69	1	9
9	0.922	$[05^1]$	0.014	0.925	0.77	1	10
10	0.957 <sup>c</sup>	$[12^{0,2}]$	0.019	0.984	1.13	1,1	12
11	1.003	$[06^{0,2}]$	0.014	1.007	1.07	1,1	14
12	1.049	$[s20^0]$	0.007	1.049	0.84		14
13	1.086	$[13^1]$	0.024	1.095	2.73	1	15

<sup>a</sup> Multiple degeneracies are listed for states with the same  $\nu_1$  and  $\nu_2$  but different  $K$  values. <sup>b</sup> At the minimum of the DORS curve just before feature 6. <sup>c</sup> At the minimum of the DORS curve just before feature 11.

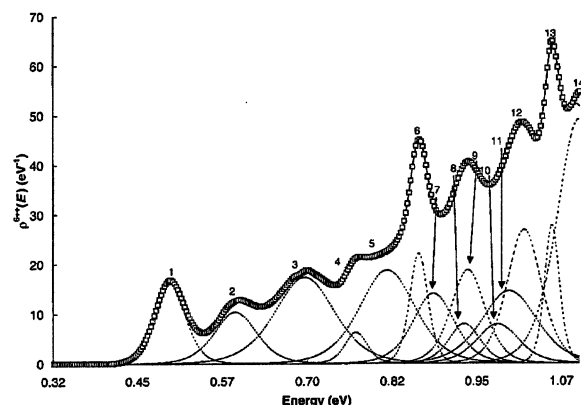


Figure 17. Line shape functions (dashed lines), their sum (solid line), and the density of reactive states (squares) as a function of the energy for  $JPS = 6++$ .

to a sum of line shape functions as before. We find that we get a good fit by using 14 terms in the sum. The line shape functions and their sum are shown in Figure 17. The  $E_{\max}$  value of each feature, the assignments, and the fit parameters of the 14 transition states are listed in Table 5. The RMS error of the fit over the range 0.32–1.1 eV is  $0.11 \text{ eV}^{-1}$ . Using the assignments for the  $JPS = 0++$ ,  $1++$ ,  $1-+$ , and  $2++$  spectra we are able to assign 13 of the 14 features in the DORS curve. We believe that feature 10, which does not appear in any of the other DORS curves, may be the supernumerary state [s12<sup>0</sup>]. It is difficult to conclusively assign feature 10, as the density of states in that region is very high and the overlap is significant. The position and the fit parameters  $\kappa_\gamma$  and  $W_\gamma$  of the feature, however, indicate that it may be due to a supernumerary transition state. Analysis of the state-specific DORS curves (which are not shown) for the product ( $1, j'$ ) and reactant ( $1, j$ ) channels indicate that there is flux in both channels. Considerably more flux, however, is seen going into the product ( $1, j'$ ) channels than is coming out of the reactant ( $1, j$ ) channel. The semiclassical energy from the VA curve for  $J = 0$  corrected for  $J = 6$  by adding the  $BJ(J + 1)$  term indicates that the product side [12<sup>0</sup>] dynamical bottleneck has an energy of about 0.84 eV. This is, however, much lower than the  $E_{\max}$  of feature 10, which is 0.976 eV.

As in the  $JPS = 2++$  spectrum, several of the features possess  $\kappa_\gamma$  values greater than 1. As explained earlier, this is due to the nonzero  $J$  value, which causes the presence of states with the same  $\nu_1$  and  $\nu_2$  values, but different  $K$  values. The

degeneracy of each state and the running sum of the degeneracies are also listed in Table 5. Again, we note that the running sum for a state at a given energy is approximately equal to the CRP at that energy up to about 1 eV.

#### IV. Discussion and Analysis

With the above assignments of stretch and bend quantum numbers to the features in the DORS curve obtained from the quantal CRP for different values of the total angular momentum  $J$ , we may conclude that the  $\text{Cl} + \text{H}_2$  reaction is controlled by quantized transition states, at least up to 1.1 eV and for  $J = 0, 1, 2$ , and 6.

**Partial Transmission Coefficients and State-Specific Processes.** To quantify the coupling between the initial or final states and the transition states, we consider the “partial transmission coefficients”  $\kappa_{\gamma\nu j}$  or  $\kappa_{\gamma\nu'j'}$  associated with a particular channel ( $\nu, j$ ) or ( $\nu', j'$ ), respectively, and a transition state  $\gamma$ . We obtain the state-specific transmission coefficients by fitting the state-specific DORS curves to a sum of line shape functions as we did for the total DORS. In this case, however, we fix the  $E_\gamma$  and the width parameters to the values obtained from the total fit and permit only the transmission coefficient parameter to vary. Figures 18a–d, 19a–d, and 20a–d show the value of the partial transmission coefficient as a function of the  $\nu$  and  $j$  (or  $\nu'$  and  $j'$ ) quantum numbers for reactants and products for  $JPS = 0++$ ,  $1++$ , and  $1-+$ . A number of the state-specific spectra show negative values for the DORS. While we performed the fit with the negative values included, Figures 18–20 omit the negative values of the partial transmission coefficients. The physical significance of the negative values of the transmission coefficients is unclear, but we may presume that it arises from interference between the various resonances. Figures 18–20 depict clearly the contributions to the transition states from the various initial and final states. It is also easy to see the various stretch adiabatic and nonadiabatic transitions from the figures.

Figure 18a shows the partial transmission coefficients as a function of the initial channel given by ( $\nu, j$ ) quantum numbers. We see that most of the transitions are strongly stretch adiabatic. Stretch nonadiabaticity occurs mostly for states that have a high degree of bend excitation. We also find a correlation between the reactants' rotational quantum number  $j$  and the bend quantum number  $\nu_2$  of the transition state. We find that for collisions that are stretch adiabatic the relation  $|j - \nu_2| \leq 3$  holds quite well for both  $J = 0$  and 1. This relation has been observed earlier<sup>3,4</sup> in other systems such as  $\text{H} + \text{H}_2$ . We see a

TABLE 5:  $E_{\max}$  Values for the Features in the DORS Curves, the Transition State Assignments, the Fit Parameters, the Degeneracy of Each Transition State, and the Running Sum of Degeneracies for  $JPS = 6++$

feature	$E_{\max}$ (eV) (DORS)	$[\nu_1\nu_2K]$	$W_\gamma$	$E_\gamma$ (eV)	$\kappa_\gamma$	degeneracies <sup>a</sup>	running sum
1	0.494	[00 <sup>0</sup> ]	0.015	0.493	0.97	1	1
2	0.596	[01 <sup>1</sup> ]	0.021	0.590	0.87	1	2
3	0.695	[02 <sup>0,2</sup> ]	0.030	0.691	2.05	1,1	4
4	0.777	[s10 <sup>0</sup> ]	0.011	0.767	0.28		4
5	0.784 <sup>b</sup>	[03 <sup>1,3</sup> ]	0.028	0.813	1.07	1,1	6
6	0.860	[10 <sup>0</sup> ]	0.009	0.859	0.79	1	7
7	0.860	[04 <sup>0,2,4</sup> ]	0.021	0.881	1.16	1,1,1	10
8	0.933	[11 <sup>1</sup> ]	0.016	0.927	0.50	1	11
9	0.933	[05 <sup>1,3,5</sup> ]	0.017	0.932	1.27	1,1,1	13
10	0.963 <sup>c</sup>	[s12 <sup>0,2</sup> ]	0.021	0.976	0.66		13
11	1.012	[12 <sup>0,2</sup> ]	0.027	0.993	1.59	1,1	15
12	1.012	[06 <sup>0,2,4,6</sup> ]	0.017	1.015	1.78	1,1,1,1	19
13	1.058	[s20 <sup>0</sup> ]	0.008	1.057	0.82		19
14	1.100 <sup>d</sup>	[13 <sup>1,3</sup> ]	0.024	1.103	5.00	1,1	21

<sup>a</sup> Multiple degeneracies listed are for states with the same  $\nu_1$  and  $\nu_2$ , but different  $K$ . <sup>b</sup> At the minimum of the DORS curve just before feature 6.

<sup>c</sup> At the minimum of the DORS curve just before feature 11. <sup>d</sup> The CRP data are available only up to 1.1 eV.

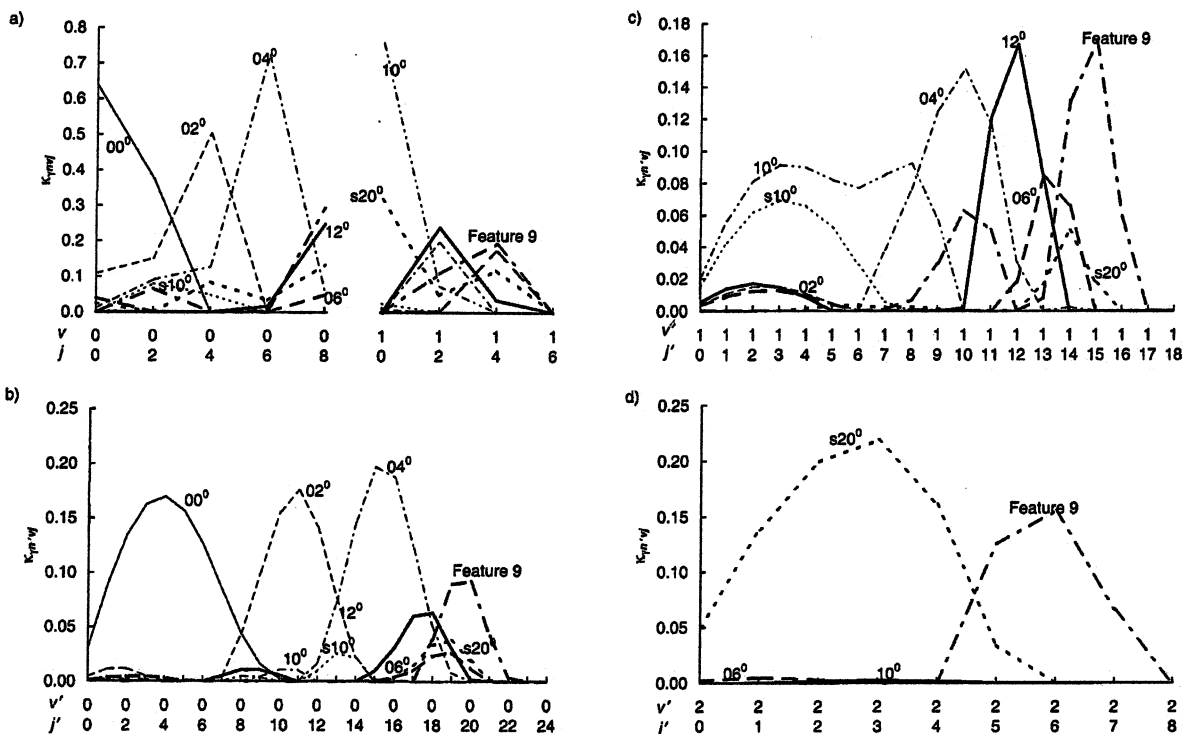


Figure 18. Partial transmission coefficients for (a)  $v' = 0, j' = 0, 2, \dots, 8$  and  $v' = 1, j' = 0, 2, \dots, 6$ , (b)  $v' = 0, j' = 0, 1, \dots, 24$ , (c)  $v' = 1, j' = 0, 1, \dots, 18$ , and (d)  $v' = 2, j' = 0, 1, \dots, 8$ . All plots are for  $JPS = 0++$ .

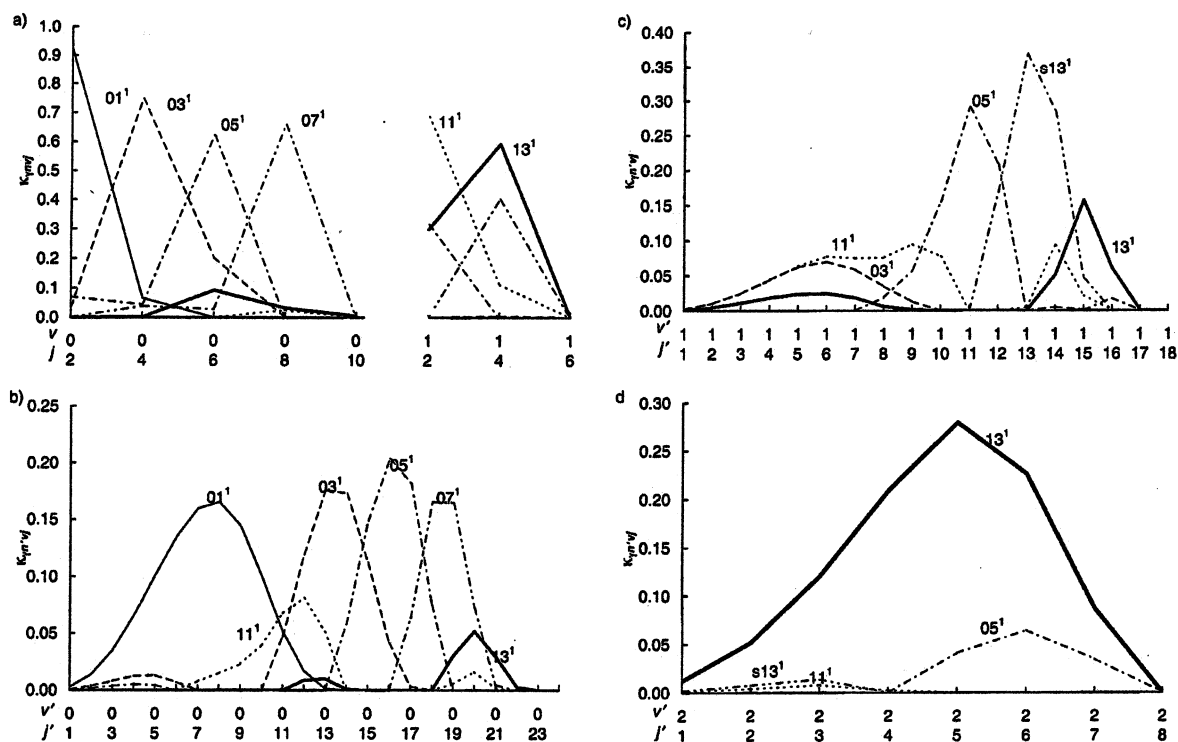
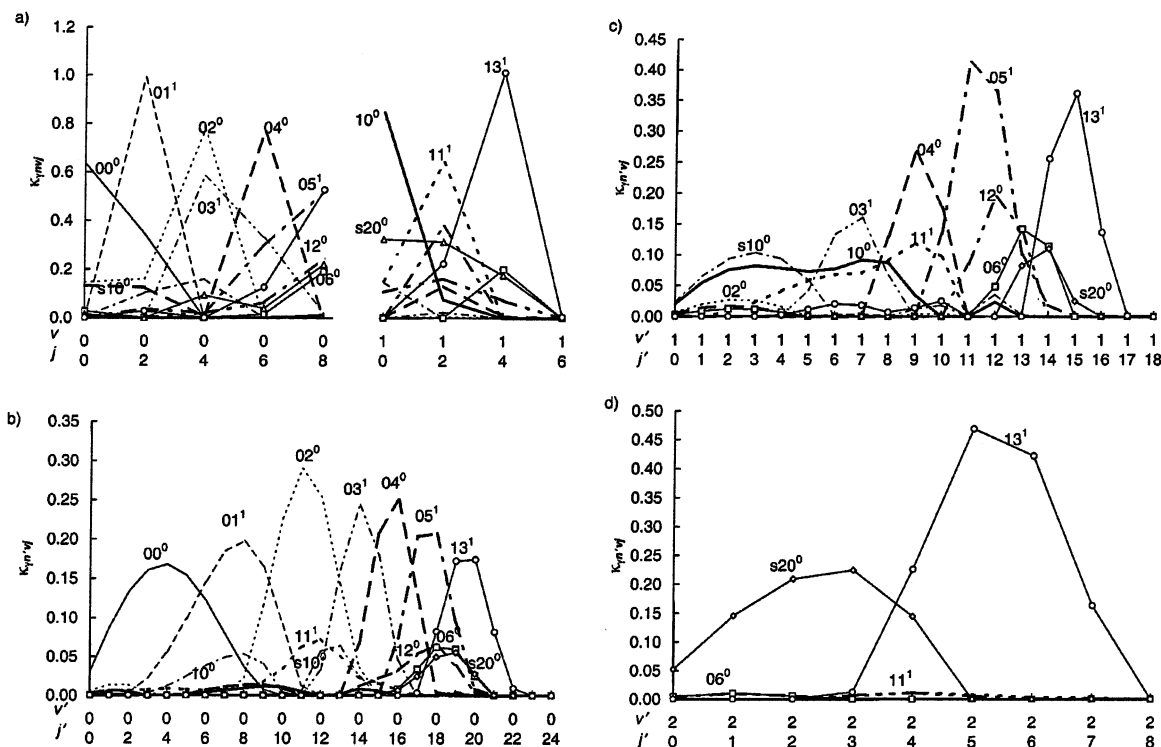


Figure 19. Partial transmission coefficients for (a)  $v' = 0, j' = 2, 4, \dots, 10$  and  $v' = 1, j' = 2, 4, 6$ , (b)  $v' = 0, j' = 1, 2, \dots, 24$ , (c)  $v' = 1, j' = 1, 2, \dots, 18$ , and (d)  $v' = 2, j' = 1, 2, \dots, 8$ . All plots are for  $JPS = 1++$ .

similar correlation in the data for  $J = 1$  as well as shown in Figures 19a and 20a. In contrast, there is no such correlation between  $j'$  and  $v_2$  or even between  $j$  and  $v_2$  for the stretch nonadiabatic transitions.

Earlier studies<sup>15,42</sup> have shown that the features in the state-specific spectra narrow as the energy is increased. This was seen<sup>15</sup> as part of a trend for greater product-state specificity as the energy of the transition state threshold increased.<sup>42</sup> Figures



**Figure 20.** Partial transmission coefficients for (a)  $\nu = 0, j = 0, 2, \dots, 8$  and  $\nu = 1, j = 0, 2, \dots, 6$ , (b)  $\nu' = 0, j' = 0, 1, \dots, 24$ , (c)  $\nu' = 1, j' = 0, 1, \dots, 18$ , and (d)  $\nu' = 2, j' = 0, 1, \dots, 8$ . All plots are for  $JPS = 1 \rightarrow +$ .

18b, 19a,b, and 20b show clearly how the transmission coefficient of a given transition state changes across the range of initial  $j$  or final  $j'$  values within a initial  $\nu$  (or final  $\nu'$ ) manifold. We see that transition states that are highly bend excited (and thus have thresholds at higher energies than the low bend excited states) tend to gate flux into a narrower range of product channels than those with low bend quantum numbers. We see that the  $\text{ClH}_2$  system shows the same product-state specificity as seen in earlier studies<sup>42</sup> on systems such as  $\text{H} + \text{H}_2$  and  $\text{O} + \text{H}_2$ .

Supernumerary states of the first kind are also clearly seen in Figures 18c–d and 20c,d. They have relatively large partial transmission coefficients in the product channels. The figures also show that transitions through the supernumerary states are substantially stretch nonadiabatic. We can also identify supernumerary states of the second kind using these figures. Parts a and c of Figure 19 show that the partial transmission coefficient for the feature corresponding to the  $[07^1]$  state has a component in the  $\nu = 1$  manifold as well a strong component in the  $\nu' = 1$  manifold. These components are possibly due to the supernumerary state  $[s13^1]$ . Since the influence of this state is not clearly seen in the total DORS but is obvious in the state-specific spectra, we may call it a supernumerary state of the second kind.

**State-Specific Rate Coefficients.** The  $JPS$ -specific thermal rate coefficient,  $k^{JPS}$ , at a temperature  $T$  for a bimolecular reaction is given by<sup>21</sup>

$$k^{JPS}(T) = \frac{B^{\text{elec}}(T) I^{JPS}(T)}{h \Phi_{\text{rel}}(T) Q_{\text{Cl}}(T) Q_{\text{HH}}(T)} \quad (7)$$

where  $B^{\text{elec}}$  is the fraction of reactants that collide on the reactive  $2A'$  surface,  $\Phi_{\text{rel}}(T)$  is the relative translational partition function of  $\text{Cl}$  with respect to  $\text{H}_2$ ,  $Q_{\text{Cl}}$  and  $Q_{\text{HH}}$  are the internal partition

functions of  $\text{Cl}$  and  $\text{H}_2$  respectively, and  $I^{JPS}$  is an integral given by

$$I^{JPS}(T) = \int_0^\infty dE \exp[-E/k_B T] N^{JPS}(E) \quad (8)$$

where  $k_B$  is Boltzmann's constant and  $N^{JPS}(E)$  is the CRP. The integral can be rewritten in terms of the density of reactive states,  $\rho^{JPS}(E)$ , as

$$I^{JPS}(T) = \int_0^\infty dE' \exp[-E'/k_B T] \int_0^{E'} dE \rho^{JPS}(E) \quad (9)$$

Equation 4 shows that we may write the DORS as a sum of contributions from the various transition states  $\gamma$ . Hence, we can write  $I^{JPS}$  as a sum over contributions from the transition states  $\gamma$

$$I^{JPS}(T) = \sum_{\gamma} I_{\gamma}^{JPS}(T) \quad (10)$$

Consequently, we can also write  $k^{JPS}$  as a sum over contributions from the various transition states  $\gamma$

$$k^{JPS}(T) = \sum_{\gamma} k_{\gamma}^{JPS}(T) \quad (11)$$

where  $k_{\gamma}^{JPS}(T)$  is the  $JPS$  and transition state-specific rate constant.

By a similar procedure, if we utilize the initial state-specific DORS,  $\rho_{n \rightarrow}^{JPS}$ , in eq 9 we can calculate the initial-state-specific rate constant,  $k_{n \rightarrow}^{JPS}(T)$ , as a sum over contributions from the various transition states.

$$k_{n \rightarrow}^{JPS}(T) = \sum_{\gamma} k_{\gamma, n \rightarrow}^{JPS}(T) \quad (12)$$

**TABLE 6:** Contribution,  $k_\gamma^{JPS}(T)$ , from Each Transition State,  $\gamma$ , as a Percentage of the Total  $JPS$ -Resolved Rate Coefficient,  $k^{JPS}(T)$ , Shown in the Last Row in Units of  $\text{cm}^3 \text{Molecule}^{-1} \text{s}^{-1}$ , at Temperatures of 300 and 800 K

[ $\gamma_1\gamma_2^K$ ]	$k_\gamma^{0++}(T)$		$k_\gamma^{1++}(T)$		$k_\gamma^{1-+}(T)$		$k_\gamma^{2++}(T)$		$k_\gamma^{6++}(T)$	
	300 K	800 K	300 K	800 K	300 K	800 K	300 K	800 K	300 K	800 K
[00 <sup>0</sup> ]	99.2	93.4			90.0	73.2	89.0	70.3	86.7	69.5
[01 <sup>1</sup> ]			96.9	91.9	4.63	17.8	4.46	16.81	4.52	16.6
[02 <sup>0</sup> ]	0.24	5.51			5.34	6.98	6.46	10.51	8.70	10.6
[03 <sup>1</sup> ]			2.38	7.00	9.9(-3)	1.00	6.2(-2)	1.22	3.7(-2)	1.76
[04 <sup>0</sup> ]	0.54	0.62			1.7(-3)	0.22	1.3(-4)	0.29	7.1(-5)	0.32
[05 <sup>1</sup> ]			3.2(-4)	0.50	5.5(-6)	0.11	2.7(-6)	9.2(-2)	6.1(-6)	0.16
[06 <sup>0</sup> ]	1.7(-8) <sup>a</sup>	7.0(-3)			1.9(-8)	7.1(-3)	1.5(-7)	3.9(-2)	3.5(-7)	6.8(-2)
[07 <sup>1</sup> ]			0.75	0.16						
[10 <sup>0</sup> ]	2.5(-5)	0.27			2.8(-5)	0.25	3.0(-5)	0.25	3.4(-5)	0.27
[11 <sup>1</sup> ]			4.2(-5)	0.38	1.9(-6)	6.9(-2)	6.0(-6)	9.9(-2)	2.5(-6)	6.7(-2)
[12 <sup>0</sup> ]	1.4(-7)	2.8(-2)			1.8(-7)	3.0(-2)	7.6(-7)	6.1(-2)	3.5(-5)	9.9(-2)
[13 <sup>1</sup> ]			1.3(-7)	5.3(-2)	2.4(-8)	2.2(-2)	1.1(-7)	3.2(-2)	1.5(-7)	5.8(-2)
[s10 <sup>0</sup> ]	1.7(-4)	0.18			3.6(-4)	0.30	3.9(-4)	0.31	4.7(-4)	0.36
[s12 <sup>0</sup> ]									1.1(-6)	4.7(-2)
[s20 <sup>0</sup> ]	1.3(-8)	1.7(-2)			1.4(-8)	1.4(-2)	1.5(-8)	1.6(-2)	1.7(-8)	1.7(-2)
na <sup>b</sup>	3.5(-9)	5.3(-3)								
$k^{JPS}(T)$	7.83(-17)	1.83(-15)	3.85(-18)	4.60(-16)	7.84(-17)	2.23(-15)	7.61(-17)	2.28(-15)	5.38(-17)	1.99(-15)

<sup>a</sup> Numbers in parentheses denote multiplicative powers of 10. <sup>b</sup> This feature was not assigned.

Table 6 shows the  $k_\gamma^{JPS}$  as a percentage of  $k^{JPS}$ , at temperatures of 300 and 800 K, for the various  $JPS$ . The table enables us to get a very detailed picture of the reaction, as we can see how much each transition state contributes to the total  $JPS$ -specific rate constant of the reaction. Several interesting trends are seen. We note that the contribution from a given state changes as the total angular momentum changes. At 300 K with  $J = 0$ , the [00<sup>0</sup>] state has almost all the contribution to the rate constant, but as  $J$  increases to 6, the contribution drops by about 15%. At 800 K the drop in the contribution from the [00<sup>0</sup>] state when  $J$  increases from 0 to 6 is about 24%. As  $J$  increases, a greater contribution to the rate constant comes from bend excited states. For a given value of  $J$ , we can expect the contribution to the rate constant to decrease monotonically as  $v_2$  increases within a given  $v_1$  manifold. This expectation is substantially borne out; however, there are exceptions, most prominently [04<sup>0</sup>] in 0++ at 300 K, [07<sup>1</sup>] in 1++ at 300 K, and [02<sup>0</sup>] in 1-+, 2+-, and 6++ at 300 K. The contributions to the rate constant from the various transition states at 800 K almost always decrease monotonically as  $v_2$  increases within a given  $v_1$  manifold. The supernumerary state has a greater contribution than the corresponding variational transition state at both temperatures considered, except for 0++ at 800 K, where the [10<sup>0</sup>] state has a greater contribution than the [s10<sup>0</sup>] supernumerary.

Parts a–c of Figure 21 show the percentage contribution to the  $JPS$ - and state-specific rate coefficient from each transition state as a function of initial rotational quantum number, for initial vibrational quantum number  $v = 0$ , with  $JPS = 0++$ , 1+-, and 1-+, respectively. The figures show that the major contribution to a given initial ( $v, j$ ) state-specific rate coefficient at a given  $JPS$  comes from few transition states in a narrow range of  $j$  values within the  $v$  manifold. Figures 18–20 showed that there is correlation between the reactants' rotational quantum number  $j$  and the bend quantum number  $v_2$  of the transition state. We find here that the same  $|j - v_2| \leq 3$  relation helps in determining which transition state (with a given  $v_2$ ) contributes substantially to the state-specific rate coefficient (for a state with rotational quantum number  $j$ ).

Parts a–c of Figure 22 show plots of the relative translational energy at the dynamical reaction thresholds for accurate quantum (solid) and VTST (dashed) as a function of the rotational quantum number of the  $v = 0$  state for various  $JPS$ . The quantal

dynamical reaction threshold is defined as<sup>4</sup> the energy at which the state-specific reaction probability first reaches a value of 0.03. The VTST dynamical reaction threshold is defined as that transition state with the lowest  $E_\gamma$  for which the partial transmission coefficient  $\kappa_{\gamma vj}$  is greater than or equal to 0.03. We see that the local maxima and minima of the solid curve are correlated with those of the dashed curve. The partial transmission coefficient for a given transition state is obtained by fitting the state-specific DORS for a certain initial ( $v, j$ ) state summed over all final states to a sum of line shape functions and is proportional to the reactive flux through that transition state from the initial ( $v, j$ ) state. This allows us to relate the partial transmission coefficient, and hence the coupling of a given initial ( $v, j$ ) state to a particular transition state, to the state-specific reactivity.

For example, Figure 22a shows that as the rotational quantum number increases from  $j = 0$  to  $j = 2$  for  $JPS = 0++$ , the relative translational energy decreases. Looking at Figure 18a, which shows us the partial transmission coefficient as a function of rotational quantum number for  $JPS = 0++$ , we see that the reactive flux out of states  $j = 0$  and  $j = 2$  is mainly focused through the [00<sup>0</sup>] state. As different reactant states with increasing  $j$  (and hence with increasing internal energy) focus reactive flux through the same [00<sup>0</sup>] state, the relative translational energy at the quantal dynamical reaction threshold decreases. When the excitation level reaches  $j = 4$ , though, the reactive flux is no longer focused through the [00<sup>0</sup>] state but rather, as Figure 18a indicates, begins to pass through the [02<sup>0</sup>] state. Since the [02<sup>0</sup>] state is higher in energy than the [00<sup>0</sup>] state, this causes the relative translational energy at the quantal dynamical reaction threshold to rise. Hence, as for the  $\text{H} + \text{H}_2$  reaction,<sup>4</sup> it is possible to explain the dependence of state-specific reactivity on the rotational quantum number by considering how strongly the specific reactant state is coupled to a given transition state.

**Rotational Constants and Geometrical Interpretation of the Dynamical Bottlenecks.** We can obtain an estimate for the rotational constants  $B_\gamma$  of the transition states  $\gamma$  by considering the  $E_\gamma$  values of the various transition states as a function of the total angular momentum  $J$ . The  $E_\gamma$  value for a given resonance is a function of  $J$  and varies by  $B_\gamma J(J + 1)$  as the total angular momentum changes.<sup>43,44</sup> As noted above, the density of reactive states increases as the total angular momen-

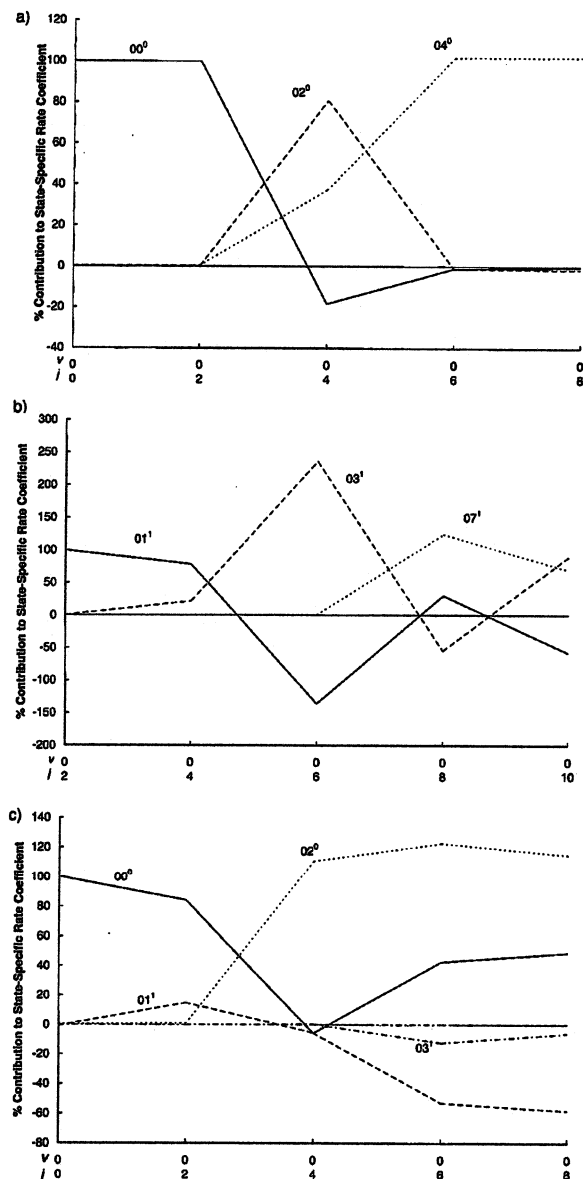


**Figure 21.** Percentage contribution to the *JPS*- and state-specific rate coefficient as a function of the rotational quantum number *j* for vibrational quantum number  $\nu = 0$  for (a) *JPS* = 0 $^{++}$ , (b) *JPS* = 1 $^{++}$ , and (c) *JPS* = 1 $^{-+}$ .

tum increases, and this tends to obscure the features in the higher total angular momentum DORS curves. We therefore chose four prominent and representative peaks that are easily distinguished in the DORS curve to obtain an estimate of the rotational constant. The states we chose were [00<sup>0</sup>], [s10<sup>0</sup>], [10<sup>0</sup>], and, a state both stretch- and bend-excited, [12<sup>0</sup>]. Table 7 shows the fitted  $E_\gamma$  values for each of these states for different values of the total angular momentum and the resulting quantal estimate for the rotational constant.

We can also obtain a value for the rotational constant from the moment of inertia  $I_\gamma$  of the structure corresponding to transition state  $\gamma$  since  $B = \hbar^2/2I$ . Figure 23 shows the VA curves for the four states considered above, the values of  $B$  along the reaction path, and the values of the distances between the three atoms involved the reaction at various points along the reaction path. From the plot of the  $B$  value versus the distance

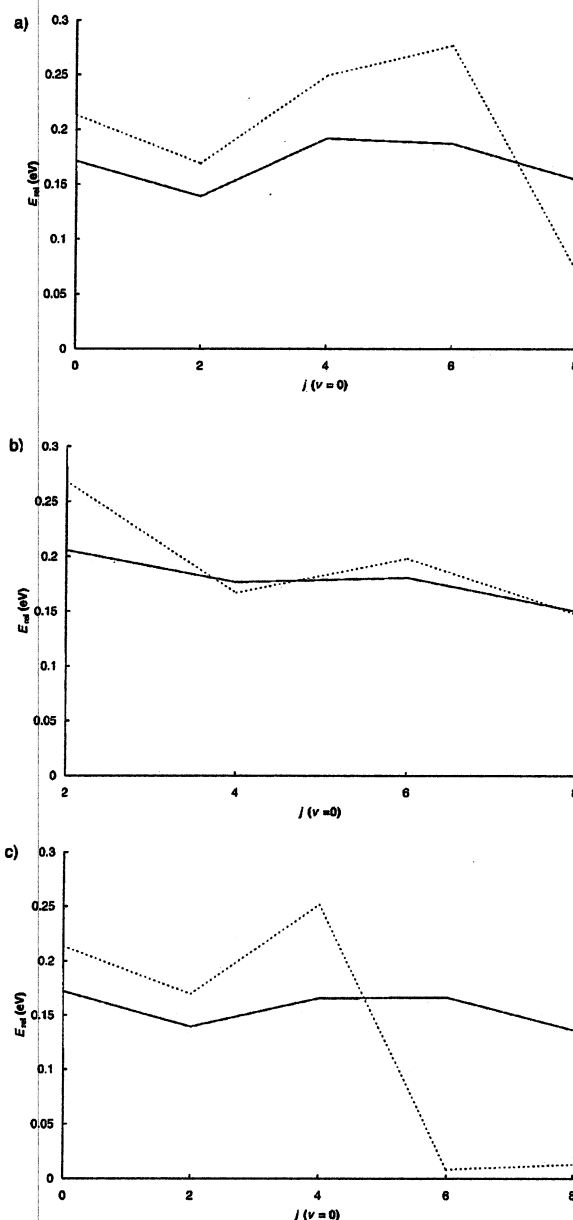


**Figure 22.** Relative translational energy at the dynamical reaction threshold as a function of the rotational quantum number *j* for vibrational quantum number  $\nu = 0$  from accurate quantum (solid) and from VTST (dashed) for (a) *JPS* = 0 $^{++}$ , (b) *JPS* = 1 $^{++}$ , and (c) *JPS* = 1 $^{-+}$ . See text for the definitions of the dynamical reaction thresholds.

from the saddle point, we see that as we get closer to the saddle point, the value of  $B$  increases; i.e., the moment of inertia decreases. This indicates that the transition state structure "tightens" as we approach the saddle point and is "looser" the further we are from it. We find that the quantal estimates of  $B$  follow this trend as well. We can calculate the moment of inertia from the geometry at the maximum of the vibrationally adiabatic curve  $V_a(\gamma, s)$ . Table 7 also shows the value of  $B$  calculated by the program ABCRATE at the dynamical bottlenecks of the VA curves for the various transition states. A state such as [12<sup>0</sup>], which is both bend- and stretch-excited, is tighter than a state such as [10<sup>0</sup>], which has no bend excitations.  $B_\gamma$  should, therefore, be larger for the tighter state, and this trend is observed in both the quantal and semiclassical estimates for  $B_\gamma$ . This

TABLE 7: Quantal Estimate for the Rotational Constant  $B$ , Along with the Value of  $B$  Calculated from the Moment of Inertia

$[\nu_1\nu_2^k]$	$J=0$ $E_\gamma$ (eV)	$J=2$ $E_\gamma$ (eV)	$J=6$ $E_\gamma$ (eV)	$B$ (eV) from $J=0$ and $6$	$B$ (eV) from $J=2$ and $6$	$B$ (eV) from ABCRATE <sup>a</sup>
$[00^0]$	0.4817	0.4834	0.4934	$2.80 \times 10^{-4}$	$2.80 \times 10^{-4}$	$2.84 \times 10^{-4}$
$[s10^0]$	0.7553	0.7568	0.7666	$2.70 \times 10^{-4}$	$2.73 \times 10^{-4}$	$2.28 \times 10^{-4}$
$[10^0]$	0.8508	0.8520	0.8591	$1.97 \times 10^{-4}$	$1.96 \times 10^{-4}$	$1.89 \times 10^{-4}$
$[12^0]$	0.9821	0.9835	0.9929	$2.57 \times 10^{-4}$	$2.62 \times 10^{-4}$	$2.12 \times 10^{-4}$

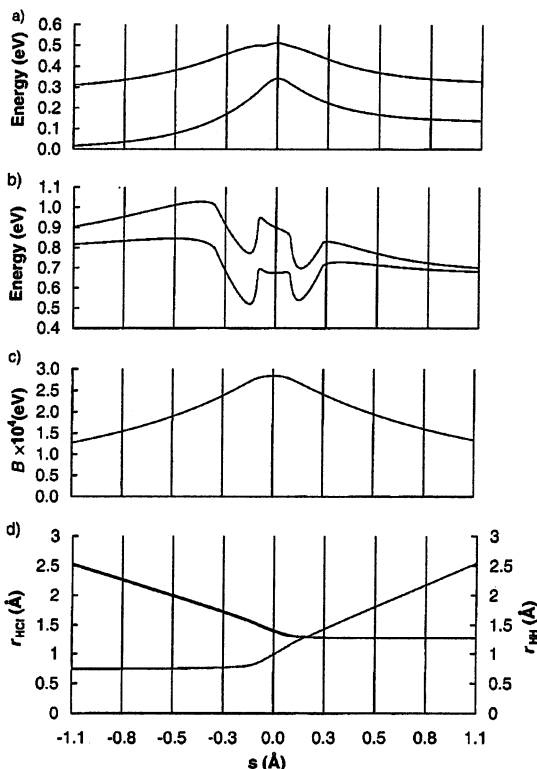
<sup>a</sup> Using the moment of inertia as calculated by ABCRATE with  $J = 0$ .

Figure 23. Reaction path properties as functions of reaction coordinate  $s$ : (a)  $V_{\text{MEP}}$  and VA curve for  $[00^0]$ ; (b) VA curves for  $[10^0]$  and  $[12^0]$ ; (c)  $B = 1/(2I)$ ; (d) H-Cl (dark line) and H-H (light line) bond distances.

provides a satisfying confirmation of the fact that the dynamical bottleneck is localized even for accurate quantal dynamics.

Since the reaction-path calculations of  $B_\gamma$  agree so well with the accurate quantal values of  $B_\gamma$ , we can use the reaction-path calculations to get insight into the geometries of the various dynamical bottlenecks. The first section of Table 8, labeled semiclassical, shows the values obtained from the maxima of the corresponding VA curves. For the second section, labeled quantal, we tabulate the values at the nearest point along the MEP that has a  $B$  value in exact agreement with the values calculated from  $J = 0$  and  $6$  in Table 7. We see that the semiclassical and quantal estimates of the geometry of the different dynamical bottlenecks agree quite well. There are, however, differences in the locations of dynamical bottlenecks as predicted by the quantum calculations and the semiclassical calculations. Thus, the semiclassical estimate of the location of the bottleneck for the  $[00^0]$  state is closer to the saddle point (a "looser" transition state) than the quantal estimate. For the stretch-excited states  $[10^0]$ ,  $[s10^0]$ , and  $[20^0]$ , however, the quantal estimates are "tighter" and the dynamical bottlenecks are predicted to be closer to the saddle point than the semiclassical estimations. This is reflected in the geometries of the

various transition states as well, as can be seen from the  $r_{\text{HH}}$  and  $r_{\text{CH}}$  distances.

**Lifetimes of the Transition States.** By considering the transition states as resonances, we can utilize the language of scattering theory, wherein we consider the resonances as poles in the  $S$  matrix.<sup>5</sup> For each transition state (or resonance)  $\gamma$ , we may write the energy of the corresponding pole in the scattering matrix as<sup>5</sup>

$$\bar{E} = E_\gamma - i \frac{\Gamma_\gamma}{2} \quad (13)$$

where  $E_\gamma$  is the real part of the energy of the resonance, and  $\Gamma_\gamma$  its width. The width is related to the lifetime  $\tau_\gamma$ , by the relation<sup>5</sup>

$$\tau_\gamma = \frac{2\hbar}{\Gamma_\gamma} \quad (14)$$

where  $\hbar$  is  $h/2\pi$ . We note that this is the lifetime at the center of the resonance, and it should not be confused with the lifetime averaged over the resonance width; the latter quantity is a factor of two smaller. For the parabolic effective energy barrier<sup>4,45</sup> assumption that we use, the lifetime is related to the width parameter,  $W_\gamma$ , as<sup>5</sup>

$$\tau_\alpha = \frac{\hbar}{\pi W_\alpha} \quad (15)$$

Table 9 shows the lifetimes of all the assigned states for the various  $JPS$  values we have considered. Examination of fits in which we varied the widths of the peaks indicates that the widths are known to about 15%, except for the  $[06^0]$  state, where the uncertainty is larger ( $\sim 30\%$ ). Certain definite trends in the values of the lifetimes are observed, and these trends involve variations larger than these uncertainties. We note that the lifetime of a particular resonance is related to the imaginary part of the energy in eq 13 by eqs 14 and 15, while the  $E_\gamma$  value of the resonance corresponds to the real part of the energy. We find that the lifetime for a particular transition state is nearly constant as the total angular momentum changes. This trend for a nearly constant lifetime as  $J$  changes can be compared to the nearly constant value for the  $E_\gamma$  of the transition state as  $J$  changes. We also see that within the  $\nu_1 = 0$  (non-stretch-excited) manifold, the lifetime first seems to decrease as  $\nu_2$  increases from 0 to 4 and then after  $\nu_2 = 4$  begins increasing again. The initial decrease in the lifetime is consistent with the non-stretch-excited VA curves which, as the bend quantum number increases, show that tunneling becomes more facile, thus increasing the width of the features and decreasing the lifetime of the transition states. We are unsure of why the lifetime would then increase after a certain level of bend excitation. Not enough stretch-excited states are present to observe the trend with the bending energy for the stretch-excited states.

The lifetimes obtained from the width parameters of the fits to the quantum data can be compared to the lifetimes obtained from the VA curves. For each transition state  $\gamma$  listed in Table



TABLE 8: Geometries and Potential Energies at Dynamical Bottlenecks

$[\nu_1\nu_2^K]$	semiclassical				quantal			
	$s$ (Å)	$r_{\text{CH}}$ (Å)	$r_{\text{HH}}$ (Å)	$V$ (eV)	$s$ (Å)	$r_{\text{CH}}$ (Å)	$r_{\text{HH}}$ (Å)	$V$ (eV)
[00 <sup>0</sup> ]	-0.01	1.41	0.98	0.511	-0.07	1.49	0.87	0.499
[s10 <sup>0</sup> ]	0.33	1.28	1.54	0.729	0.13	1.30	1.23	0.541
[10 <sup>0</sup> ]	-0.53	2.00	0.75	0.846	-0.48	1.95	0.75	0.845
[12 <sup>0</sup> ]	0.27	1.28	1.44	0.830	0.19	1.29	1.32	0.741

TABLE 9: Lifetimes (fs) of the Transition State Resonances for Various  $JPS$  from Quantum Results and the Comparison to Lifetimes from the Semiclassical Vibrationally Adiabatic Curves<sup>a</sup>

$[\nu_1\nu_2^K]$	0++	1++	1-+	2++	6++	semiclassical <sup>b</sup>
[00 <sup>0</sup> ]	14		14	14	14	8.6
[01 <sup>1</sup> ]		10	10	10	10	8.5
[02 <sup>0</sup> ]	9		7	7	7	6.2
[03 <sup>1</sup> ]		7	7	7	8	5.6
[04 <sup>0</sup> ]	6		7	9	10	5.1
[05 <sup>1</sup> ]		9	10	15	12	4.7
[06 <sup>0</sup> ]	26		25	15	12	4.4
[07 <sup>1</sup> ]		5				4.2
[10 <sup>0</sup> ]	27		25	25	23	34.0
[11 <sup>1</sup> ]		16	16	11	14	21.8
[12 <sup>0</sup> ]	16		16	11	9	15.7
[13 <sup>1</sup> ]		13	10	9	10	12.1
[s10 <sup>0</sup> ]	28		22	21	19	20.3
[s12 <sup>0</sup> ]					10	9.7
[s20 <sup>0</sup> ]	30		30	28	28	36.1

<sup>a</sup> The lifetimes in the five columns headed by  $JPS$  are from the accurate quantal calculations. <sup>b</sup> These results are for  $J = 0$  and are obtained from calculations of VA curves performed using ABCRATE.

9, we fit a segment of the VA curve that extends approximately  $\pm 0.01$  Å on each side of the dynamical bottleneck to a parabolic function

$$V_a(\gamma, s) = V_\gamma^0 - \frac{1}{2} k_\gamma (s - s_\gamma^0)^2 \quad (16)$$

where  $V_a(\gamma, s)$  is the vibrationally adiabatic energy,  $V_\gamma^0$  is the maximum of the VA curve in the region of the dynamical bottleneck,  $k_\gamma$  is a force constant (defined here as the negative of the usual force constant),  $s$  is the distance along the reaction path, and  $s_\gamma^0$  is the position of the dynamical bottleneck along the reaction path. Using a quantum mechanical analysis of the tunneling through an effective potential barrier,<sup>4,45</sup> it can be shown that the parameter  $k_\gamma$  is related to the width parameter  $W_\gamma$  by the relation

$$W_\gamma = \frac{\hbar}{2\pi} \sqrt{\frac{k_\gamma}{\mu}} \quad (17)$$

where  $\mu$  is the reduced mass of the isoinertial coordinate system in which  $V_a(\gamma, s)$  is expressed. We then calculate the lifetime using eq 15. The final column of Table 9 lists the lifetimes calculated using the semiclassical VA curves for zero total angular momentum. We see that the semiclassical lifetimes are in reasonably good agreement with most of the quantal estimates. We note, however, that the semiclassical lifetimes in the  $\nu_1 = 0$  manifold monotonically decrease with increasing  $\nu_2$ , while the quantal lifetimes in the same manifold decrease and then increase after  $\nu_2 = 4$ .

## V. Conclusions

The analysis of rate constants in terms of the energies, lifetimes, and transmission coefficients of quantized transition states provides the finest level of detail allowed by quantum

mechanics. In this paper we have analyzed the accurate quantal microcanonical-ensemble rate constants for the Cl + H<sub>2</sub> reaction by resolving and characterizing the quantized features in the cumulative reaction probabilities that contain all the dynamical information in these rate constants. We examined total energies up to 1.1 eV and total angular momentum in the range  $J = 0$  to  $J = 6$ . We find in all cases that the reaction is controlled by the quantized nature of the transition state energy levels. We have assigned the energy level spectrum for the transition state region of this atom-diatom system by assuming it to be a triatomic system with a missing degree of freedom, which is the reaction coordinate at the transition state. We find that the assumption of local vibrational adiabaticity is useful for labeling the levels of the transition state, although, as for H + H<sub>2</sub> and O + H<sub>2</sub>, the reaction is not globally vibrationally adiabatic. We analyzed the state-specific reaction probabilities as well, from which we obtain a detailed picture of the state-to-state reactivity of the system.

We also calculated the  $JPS$ -specific and state-specific rate coefficients for the Cl + H<sub>2</sub> reaction for  $JPS = 0++$ ,  $1++$ , and  $1-+$ . Examination of the contribution from each transition state to the  $JPS$ -specific rate coefficient as a function of the reactant's rotational quantum number allows us to explain the dependence of the state-specific reactivity on the reactant's rotational quantum number in terms of the coupling of a particular reactant state to a specific transition state.

Sometimes there are two sets of resonances with the same sets of quantum numbers. We assign these to metastable states centered at different positions along the reaction path. The higher-energy one is called a variational transition state resonance, and the lower-energy one is called a supernumerary transition state resonance. All transition state resonances affect at least one state-selected reaction probability; they vary in their effect on the total reaction probability. All variational transition state resonances and some supernumerary transition state resonances (these are called supernumeraries of the first kind) have nonzero transmission coefficients  $\kappa$  for the total reactive flux, and one can identify a continuous range of  $\kappa$  values from almost zero to about unity. Those supernumeraries for which the  $\kappa$  associated with the total reactive flux is essentially zero (too small for us to observe their effect) are called supernumeraries of the second kind. In this paper we assigned vibrational quantum numbers  $\nu_1$  and  $\nu_2$  to twelve different variational transition state resonances, three different supernumeraries of the first kind, and one supernumerary of the second kind. Of the twelve variational transition state resonances, six were identified for four of the  $JPS$  blocks, namely  $JPS = 0++$ ,  $1-+$ ,  $2++$ , and  $6++$ , five were identified for  $JPS = 1-+$ ,  $1++$ ,  $2++$ , and  $6++$ , and one was identified only for  $JPS = 1++$ . Of the three supernumeraries of the first kind, two were identified for  $JPS = 0++$ ,  $1-+$ ,  $2++$ , and  $6++$ , and one was identified only for  $JPS = 6++$ . The supernumerary of the second kind was identified only for  $JPS = 1++$ .

By comparing the energetic positions of the resonances for different total angular momentum, we have obtained an estimate for the rotational constant  $B$  for four of the transition state energy

levels, including three variational transition states and one supernumerary transition state. The variation in the value of the rotational constant between the various transition states indicates the shift in the dynamical bottleneck of the reaction for various stretch and bend excitations. The estimates of the rotational constant from the  $J$  dependence of transition state resonance energies compare favorably with the estimates from the moments of inertia, and this allows us to infer the geometries of the various dynamical bottlenecks.

The widths of the features in the transition state spectrum provide estimates of the transition state lifetimes, which range from 6 to 30 fs. These may be compared to values of 5 to 36 fs obtained from a parabolic tunneling analysis employing the vibrationally adiabatic potential energy curves. The vibrationally adiabatic potential curves provide a semiquantitative rationalization of the lifetimes of the variational transition states, but they do not explain the nonmonotonic dependence of lifetime on the bend quantum number.

**Acknowledgment.** We thank Yuri Volobuev, Michael Hack, and Steven Mielke for helpful discussions and comments. This work was supported in part by the National Science Foundation under Grant No. CHE97-25965.

## References and Notes

- (1) (a) Haug, K.; Schwenke, D. W.; Truhlar, D. G.; Zhang, Y.; Zhang, J. Z. H.; Kouri, D. J. *J. Chem. Phys.* **1987**, *87*, 1892. (b) Bowman, J. M. *Chem. Phys. Lett.* **1987**, *141*, 545.
- (2) Chatfield, D. C.; Friedman, R. S.; Truhlar, D. G.; Garrett, B. C.; Schwenke, D. W. *J. Am. Chem. Soc.* **1991**, *113*, 486.
- (3) Chatfield, D. C.; Friedman, R. S.; Truhlar, D. G.; Schwenke, D. W. *Faraday Discuss. Chem. Soc.* **1991**, *91*, 289.
- (4) Chatfield, D. C.; Friedman, R. S.; Schwenke, D. W.; Truhlar, D. G. *J. Phys. Chem.* **1992**, *96*, 2414.
- (5) Chatfield, D. C.; Friedman, R. S.; Mielke, S. L.; Lynch, G. C.; Allison, T. C.; Truhlar, D. G.; Schwenke, D. W. In *Dynamics of Molecules and Chemical Reactions*; Wyatt, R. E., Zhang, J. Z. H., Eds.; Marcel Dekker: New York, 1996; p 323.
- (6) Truhlar, D. G.; Garrett, B. C.; Klippenstein, S. J. *J. Phys. Chem.* **1996**, *100*, 12771.
- (7) Moore, C. B.; Smith, I. W. M. *J. Phys. Chem.* **1996**, *100*, 12848.
- (8) Newton, R. G. *Scattering Theory of Waves and Particles*, 2nd ed.; Springer-Verlag: New York, 1982.
- (9) Taylor, J. R. *Scattering Theory*; John Wiley & Sons: New York, 1972.
- (10) Seideman, T.; Miller, W. H. *J. Chem. Phys.* **1991**, *95*, 1768.
- (11) Friedman, R. S.; Truhlar, D. G. *Chem. Phys. Lett.* **1991**, *183*, 539.
- (12) (a) Pollak, E.; Pechukas, P. *J. Chem. Phys.* **1978**, *69*, 1218. (b) Gomez Llorente, J. M.; Borondo, F.; Berenguer, N.; Benito, R. M. *Chem. Phys. Lett.* **1992**, *192*, 430. (c) Burghardt, I.; Gaspard, P. *J. Phys. Chem.* **1995**, *99*, 2732. (d) Sepulchre, J.-A.; Gaspard, P. *J. Chem. Phys.* **1995**, *102*, 6727.
- (13) Friedman, R. S.; Hunniger, V. D.; Truhlar, D. G. *J. Phys. Chem.* **1995**, *99*, 3184.
- (14) Marston, C. C.; Wyatt, R. E. *ACS Symp. Ser.* **1984**, *263*, 441.
- (15) Chatfield, D. C.; Friedman, R. S.; Lynch, G. C.; Truhlar, D. G.; Schwenke, D. W. *J. Chem. Phys.* **1993**, *98*, 342.
- (16) Chatfield, D. C.; Friedman, R. S.; Lynch, G. C.; Truhlar, D. G. *J. Phys. Chem.* **1992**, *96*, 57.
- (17) Klippenstein, S. K.; Kress, J. D. *J. Chem. Phys.* **1992**, *96*, 8164.
- (18) (a) Kress, J. D.; Klippenstein, S. K. *Chem. Phys. Lett.* **1992**, *195*, 513. (b) Kress, J. D.; Walker, R. B.; Hayes, E. F.; Pendergast, P. *J. Chem. Phys.* **1994**, *100*, 2728.
- (19) Allison, T. C.; Mielke, S. L.; Schwenke, D. W.; Lynch, G. C.; Gordon, M. S.; Truhlar, D. G. In *Gas-Phase Chemical Reaction Systems*; Wolfrum, J., Volpp, H.-R., Ranacher, R., Warnatz, J., Eds.; Springer: Berlin, 1996; p 111.
- (20) Allison, T. C.; Lynch, G. C.; Truhlar, D. G.; Gordon, M. S. *J. Phys. Chem.* **1996**, *100*, 13575.
- (21) Mielke, S. L.; Allison, T. C.; Truhlar, D. G.; Schwenke, D. W. *J. Phys. Chem.* **1996**, *100*, 13588.
- (22) Alagia, M.; Balucani, N.; Cartechini, L.; Casavecchia, P.; van Kleef, E. H.; Volpi, G. G.; Aoiz, F. J.; Banières, L.; Schwenke, D. W.; Allison, T. C.; Mielke, S. L.; Truhlar, D. G. *Science* **1996**, *273*, 1519.
- (23) Sun, Y.; Kouri, D. J.; Truhlar, D. G.; Schwenke, D. W. *Phys. Rev. A* **1990**, *41*, 4857.
- (24) Schwenke, D. W.; Mielke, S. L.; Truhlar, D. G. *Theor. Chim. Acta* **1991**, *79*, 241.
- (25) Mielke, S. L.; Truhlar, D. G.; Schwenke, D. W. *J. Chem. Phys.* **1991**, *95*, 5930.
- (26) Tawa, G. J.; Mielke, S. L.; Truhlar, D. G.; Schwenke, D. W. In *Advances in Molecular Vibrations and Collision Dynamics*; Bowman, J. M., Ed.; JAI Press: Greenwich, CT, 1994; Vol. 2B, p 45.
- (27) Tawa, G. J.; Mielke, S. L.; Truhlar, D. G.; Schwenke, D. W. *J. Chem. Phys.* **1994**, *100*, 5751.
- (28) Press, W. H.; Teukolsky, S. A.; Vetterling, W. T.; Flannery, B. P. *Numerical Recipes in Fortran*, 2nd ed.; Cambridge University Press: Cambridge, U.K., 1992; p 107.
- (29) Herzberg, G. *Molecular Spectra and Molecular Structure*; Van Nostrand: Princeton, 1945; Vol. 2, p 80.
- (30) Eliason, M. A.; Hirschfelder, J. R. *J. Chem. Phys.* **1959**, *30*, 1426.
- (31) Marcus, R. A. *J. Chem. Phys.* **1967**, *46*, 959.
- (32) Truhlar, D. G. *J. Chem. Phys.* **1970**, *53*, 2041.
- (33) Garrett, B. C.; Truhlar, D. G. *J. Phys. Chem.* **1982**, *86*, 1136.
- (34) Garrett, B. C.; Truhlar, D. G.; Grev, R. S.; Magnuson, A. W. *J. Phys. Chem.* **1980**, *84*, 1730; **1983**, *87*, 4554 (E).
- (35) Garrett, B. C.; Truhlar, D. G. *J. Phys. Chem.* **1979**, *83*, 1052.
- (36) Garrett, B. C.; Lynch, G. C.; Allison, T. C.; Truhlar, D. G. *Comput. Phys. Commun.* **1998**, *47*, 109.
- (37) Landau, L. D.; Lifshitz, E. M. *Quantum Mechanics*, 2nd ed.; Pergamon: Oxford, U.K., 1965; p 163.
- (38) Garrett, B. C.; Truhlar, D. G. *J. Chem. Phys.* **1984**, *81*, 309.
- (39) Natanson, G. A. *J. Chem. Phys.* **1990**, *93*, 6589.
- (40) Garrett, B. C.; Truhlar, D. G. *J. Chem. Phys.* **1991**, *95*, 10374.
- (41) Marcus, R. A. *Discuss. Faraday Soc.* **1967**, *44*, 7.
- (42) Chatfield, D. C.; Truhlar, D. G.; Schwenke, D. W. *J. Chem. Phys.* **1992**, *96*, 4313.
- (43) Redmon, M. J.; Wyatt, R. E. *Chem. Phys. Lett.* **1979**, *63*, 209.
- (44) Pollak, E. *J. Phys. Chem.* **1986**, *90*, 3619.
- (45) Skodje, R. T.; Truhlar, D. G. *J. Phys. Chem.* **1981**, *85*, 624.